original draft
Aug 10, 2012 – 3 PM

Proposal for an Accelerator R&D User Facility at Fermilab's Advanced Superconducting Test Accelerator (ASTA)

Fermilab

U.S. DEPARTMENT OF ENERGY

Managed by Fermi Research Alliance, LLC for the Department of Energy

Table of Contents

1.0 Executive Summary 4
2.0 ASTA Facility Overview and Capabilities 5
3.0 Scientific Opportunities at ASTA 8
3.1 Scientific Drivers in Advanced Accelerator R&D 8
3.2 Fermilab's historical contributions in AARD 8
3.3 Comparison with other AARD Facilities 8
3.4 High-brightness X-ray channeling radiation source 8
3.4.1 Introduction: Channeling radiation as a ultra-bright X-ray source 8
3.4.2 Experimental plans at ASTA 12
3.4.3 Other spin-off opportunities 12
3.5 Advanced phase space manipulations 13
3.5.1 Transformative applications of advanced phase space manipulations 13
3.5.2 Flat beam transformation 14
3.5.3 Transverse-to-longitudinal phase space exchange 16
3.5.4 Transverse-to-longitudinal phase space exchange at ~700 MeV 20
3.6 Integrable-optics test accelerator (IOTA) ring construction and operation 22
3.6.1 Introduction 22
3.6.2 Concept of nonlinear integrable optics 22
3.6.3 IOTA goals and scope 27
3.6.4 IOTA Design 28
3.6.5 Status and Schedule 32
3.7 Attosecond vacuum-ultraviolet pulses via space-charge-driven amplification of shot-noise density fluctuations 33
3.8 Potential for Critical Laser-Induced Microbunching Studies with the High-Micropulse-Repetition-Rate Electron beams at ASTA – updated 7/24 35
3.8.1 Abstract 35
3.8.2 Introduction 35
3.8.3 Laser-Induced Microbunching 37
3.8.4 Coherent Optical Transition Radiation 38
3.8.5 Proposed studies 41
3.8.6 Phase 1 42
3.8.7 Phase 2 43

3.8.8 Summary 45
3.8.9 References 45
3.9 Feasibility of an XUV FEL Oscillator at ASTA – new 7/26 46
3.9.1 Abstract 46
3.9.2 Introduction 46
3.9.3 Conceptual Aspects of Undulator Radiation 47
3.9.4 Proposed Studies 49
3.9.5 Application 1: Diagnostics Undulator 49
3.9.6 Application 2: XUV FEL Oscillator 51
3.9.7 Practical Considerations 55
3.9.8 Summary 56
3.9.9 Acknowledgements 57
3.9.10 References 57
3.10 Production of narrow-band gamma rays 58
3.11 Synergies with the MAtter-Radiation Interaction at the Extreme (MARIE) project at Los Alamos 58
3.12 Beam-Beam Kickers for ELIC at JLab 59
3.13 Radiabeams on Gamma-Source 59
3.14 Space Charge Compensation 59
3.15 Demonstration of Technology and Beam Parameters of an ILC RF-unit 59
3.16 Miscellaneous Expressions of Interest 59
4.0 The Fermilab Context 59
5.0 Technical Description of ASTA 60
6.0 Accelerator Science Education at ASTA 60
7.0 Scope, Cost and Schedule 60
8.0 Operating Budget 60
8.1 Assumptions 60
9.0 Management of the Scientific User Program 60
10.0 List of Acronyms – new 7/30 61
11.0 Appendix 1: Letters of Support 62
12.0 References – apparently this must be last to work! 62

1.0 Executive Summary

Construction of the Advanced Superconducting Test Accelerator (ASTA) Facility at NML began in 200X as part of the American Recovery and Reinvestment Act (ARRA) and International Linear Collider R&D Program within the Department of Energy, Office of High Energy Physics. Construction of the facility was motivated by the goal of building, testing and operating a complete ILC RF unit to demonstrate industrial and laboratory capability for producing state-of-the-art superconducting linear accelerator components, and assembling them into a fully functioning system. ASTA, configured as a single ILC RF unit, would consist of an electron photo-injector, accelerating cavities, a bunch compressor, and three 1.3 GHZ ILC cryomodules powered together from a single high-power klystron. Each cryomodule provides 250 MeV of energy gain for a total output energy of approximately 750 MeV.

It was recognized early in the planning process that an electron beam meeting the demanding ILC performance parameters was itself a powerful resource of interest to the wider Advanced Accelerator R&D community. For those reasons the ARRA-funded facility construction incorporated space for the installation of additional cryomodules to increase the beam energy to a maximum of 1.5 GeV, space for multiple high-energy beamlines, as well as provision for a small circular ring for the exploration of advanced accelerator concepts. The facility design incorporated features necessary for the operation of an AARD user program, including adequate experimental beamline and insertion space, an appropriately sized support building, provision for transporting laser light into and out of the accelerator enclosure, and an adequately-sized control room.

It was anticipated that initial operation of the facility would be focused on demonstrating ILC performance. Once completed, it was expected that the facility would be made available to the world-wide AARD user community and operated as a user-facility in support of a broad program in accelerator science.

With the completion of the ILC R&D Program in FY2012, DOE/OHEP has directed Fermilab to cease construction of the ASTA facility at NML. This Proposal is submitted in recognition of the tremendous opportunity that the ASTA facility, based on a state-of-the-art superconducting linear accelerator, represents to the national and international Advanced Accelerator R&D user community.

The ASTA facility at NML presently consists of the following:

- An XX-meter long, XX-ft^2 shielded accelerator enclosure housed inside the XX-ft^2 NML building.
- An XX-ft^2 support building
- A control room
- An operating radio-frequency photo-injector system, including the drive laser system
- Operating high-power and low-level RF systems, RF distribution system and controls
- Refrigeration system capable of XX/YY.

Two cryomodules have been assembled and a third is presently under construction. Parts, including cavities, couplers, …, for a total of XX cryomodules have been purchased. ASTA experimental beamline equipment, including XX quadrupoles, XX vacuum chambers, XX beam position monitors, etc. have been purchased.

The ARRA-funded construction of the NML facility has been completed at a total investment of approximately XM$. Further facility construction costs total XM$. The construction of two cryomodules has been completed, and the construction of a third is underway. To date, a total of XM$ has been spent to construct the ASTA facility, and XM$ has been spent on the ASTA accelerator systems. It is estimated that XM$ is required to complete the ASTA facility, and XM$ is required to complete the ASTA accelerator and beamlines. An additional XM$ is required to complete the Integrable Optics Test Accelerator, a 30-m circumference ring designed for the study of novel, non-linear accelerator lattices. With this Proposal we request funds totaling XXM$ for the completion of ASTA, and provide an estimate of the annual cost of operating a user program at ASTA of XXM$.

The completion of ASTA and operation of a user program builds upon Fermilab's strong history in experience in the operation of the A0 photoinjector and its associated R&D program. That program has produced XX Ph.Ds in accelerator science since its inception in 199X. The scientific strength of that program and the assembled staff who operate it and direct the R&D program has resulting, just in the last two years, in XX high-quality publications in accelerator science. With the substantial investment already made in the ASTA facility, and the additional funds requested to compete the facility, OHEP has the opportunity to support a unique, state-of-the-art, modern AARD user facility which has the capability of supporting a vibrant user-driven accelerator science research program which will develop transformative approaches to particle-beam acceleration, particle-beam manipulation, and photon-beam generation.

Accelerator R&D has played a crucial role in enabling scientific discovery in the past century and will continue to play this role in the years to come. In the U.S., the Office of High Energy Physics within DOE's Office of Science is developing a plan for national accelerator stewardship. ASTA offers the possibility for DOE/OHEP to strengthen its stewardship portfolio through the establishment of a national accelerator science user facility based on the unique capabilities afforded by state-of-the-art superconducting linear accelerator technology. The scientific research carried out at ASTA is expected to have a broad impact, influencing fields from particle physics to basic-energy sciences to national security. As the nation's particle physics laboratory, Fermilab intends to play a leading role in the development of tomorrow's accelerators. A key element of that vision is a world-leading user facility for accelerator science.

2.0 ASTA Facility Overview and Capabilities

The backbone of the ASTA facility is a radio-frequency (RF) photoinjector; see Fig. 1. The photoinjector comprises a 1-1/2 cell cylindrical-symmetric RF gun [1] with a semiconductor photocathode located on its back plate; see Fig. 1 The cathode is illuminated by an ultraviolet (UV, λ=266 nm) laser pulse produced via frequency quadrupling of an amplified infrared (IR, λ=1024 nm) pulse [2]. The photocathode drive laser enables the generation of a train of bunches repeated at 3 MHz within a 1-ms-duration macropulse. The parameters associated to the pulse format are summarized in Table 1. The 4-MeV electron bunches exiting the RF gun are then accelerated with two superconducting radio-frequency (SRF) TESLA-type cavities (CAV1 and CAV2) to approximately 40 MeV. Downstream of this accelerating section the beamline includes diverse magnetic elements such as quadrupole and steering dipole magnets, along with a four-bend magnetic compression chicane (BC1). The beamline also incorporates a round-to-flat-beam transformer (RTFB) capable of manipulating the beam such to generate a high transverse-emittance ratio. In the early stages of operation, the bunches will be compressed in BC1 by operating CAV2 off crest. In this scenario the longitudinal phase space is strongly distorted and the achievable peak current limited. Eventually a third-harmonic cavity (CAV39) operating at 3.9 GHz will be added. The prime purpose of this cavity is to linearize the longitudinal phase and thereby enhance the compression scheme. In addition such a cavity could also be used to shape the current profile of the electron bunch [3]. The bunch generation and acceleration was extensively simulated and optimized using a multi-objective genetic optimizer [4].

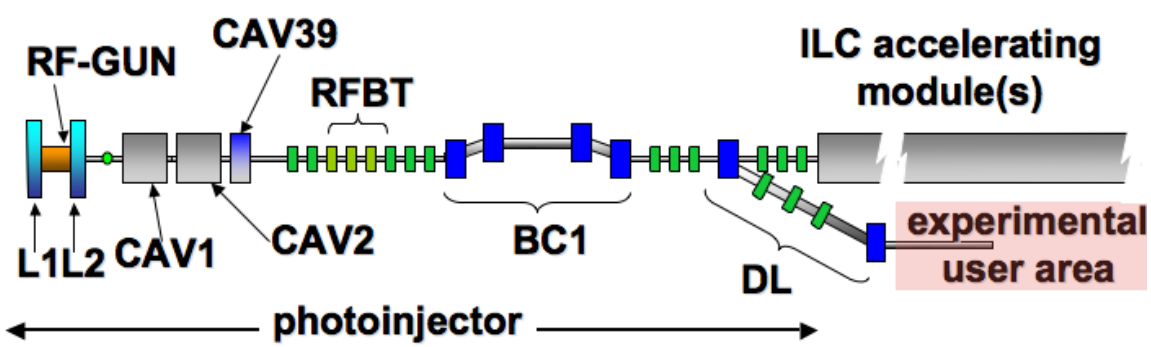

Figure 1: Overview of the ASTA photoinjector. The legend is L1, L2: solenoidal lenses, CAV1, CAV2 superconducting TESLA cavities, CAV39, 3rd harmonic accelerating cavity, BC1: magnetic bunch compressor, DL: dogleg, green rectangles: quadrupoles magnets, RFBT: round-to-flat-beam transformer.

Downstream of the accelerating section, the photoinjector includes an extensive diagnostics suite. Beside conventional diagnostics (optical transition radiation screens, frequency-domain bunch-length measurement, etc…), a deflecting cavity with a spectrometer will provide single-shot measurement of the longitudinal phase space (LPS diagnostics). Further developments of single-shot electro-optical imaging method initiated at the A0 photoinjector is also planned downstream of BC1 [5].

The photoinjector also include an off-axis experimental beamline branching off at the second dipole of BC1 that will support beam physics experiments and diagnostics R&D.

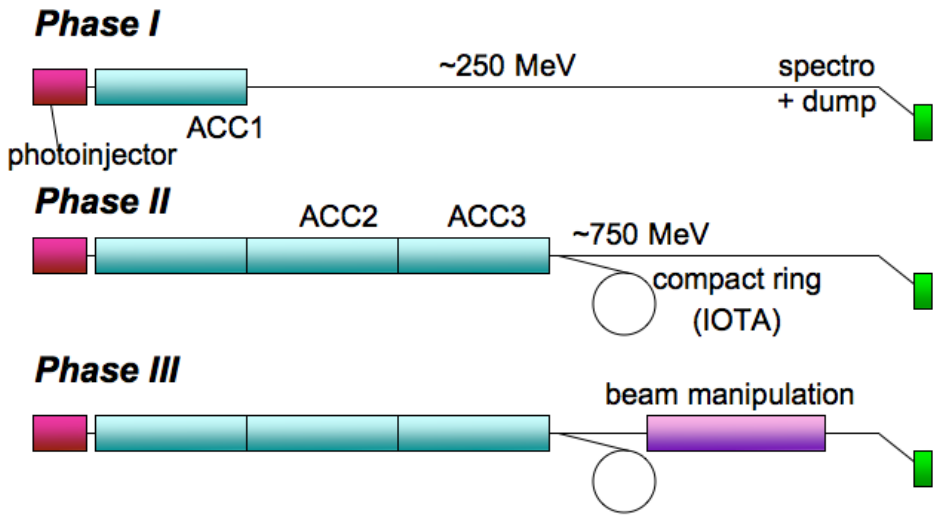

Figure 2: Phases for the ASTA construction/operation.

Table 1: Electron beam pulse format

Parameter	Value	Unit
Bunch charge	0.02 – 3.2	nC
Bunch train duration	1	ms
Bunch frequency with train	3	MHz
Number of bunches/train	1-3000	
Bunch train frequency	5	Hz

Nominally, the 40-MeV beam is sent to a string of superconducting accelerating modules (each cryomodule comprises 8 SRF cavities). The installation of the cryomodules will be staged pending the completion of their construction as depicted in Fig. 2.

During the first-beam operation and commissioning (referred to as Phase I), only one cryomodule will be installed allowing for the production of bunches with energies up to ~250 MeV. Eventually, a second (Phase II) and third (Phase III) cryomodules will be installed.

Together, the three cryomodules plus the radio frequency (RF) power systems will make up one complete RF unit for ILC R&D. During Phase III operation the beam energy will approximately reach 750 MeV. Beyond Phase III several options are currently under consideration, one of them could be the installation of a 4th cryomodule downstream of a phase-space-manipulation beamline (either a simple bunch compressor or a phase space exchanger similar to the ones discussed below).

3.0 Scientific Opportunities at ASTA

3.1 Scientific Drivers in Advanced Accelerator R&D

3.2 Fermilab's historical contributions in AARD

3.3 Comparison with other AARD Facilities

3.4 High-brightness X-ray channeling radiation source

The quest for short-wavelength compact light source has been driven by applications ranging from fundamental science to homeland security. Recently, Vanderbilt and Northern Illinois University received funding to work on the development of compact X-ray radiation source. The proposal aims at producing x-rays using a 40-MeV electron beam. A proof-of-principle experiment is foreseen in the ASTA photoinjector area. This section is based on the proposed concept detailed in Ref. [6].

3.4.1 Introduction: Channeling radiation as a ultra-bright X-ray source

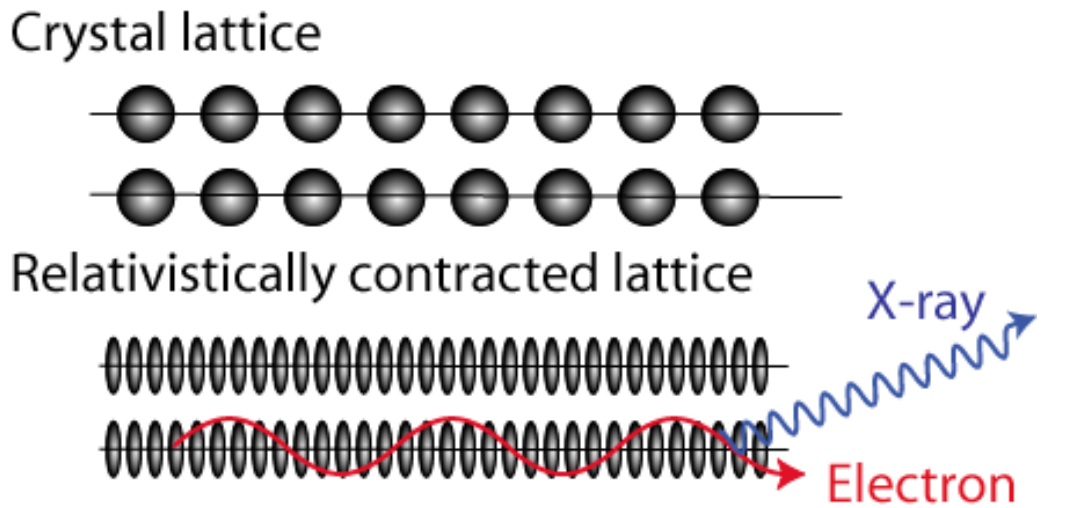

Figure 3: Mechanism of channeling radiation production.

In a crystal, the ions in each crystal plane form a sheet of positive charge. When a relativistic electron travels through the crystal parallel to the crystal plane, Lorentz contraction increases the charge density by the factor γ and the electron oscillates about the crystal plane in quantum states normal to the plane, as depicted in Fig. 3. Radiation from transitions between the quantum states is called channeling radiation. Channeling radiation was predicted theoretically by Kumakhov [7] in 1974, and experimentally observed by Terhune and Pantell [8] in 1975. Since then, there has been extensive theoretical and experimental investigation of channeling radiation, and theory and experiment are in good agreement.

The transverse forces experienced by an electron traveling along a crystal plane are comparable to those in a 10^4-T magnetic undulator or a 1-TW laser undulator focused to a 10-μm spot. The equivalent "undulator period" is on the order of 0.1 μm. The coherence length of the crystal "undulator" is limited by scattering to the order of 1 μm, so the number of "undulator periods" in channeling radiation is on the order of 10. The photon yield is more than 10 photons per electron at high energy (GeV), but on the order of 10^{-4} photons per electron in the x-ray region [9]. The channeling-radiation peaks are typically an order of magnitude above the bremsstrahlung background [10]. The advantages of a channeling radiation source are clear. Compared with a conventional undulator, channeling radiation requires only a 40-MeV electron beam, rather than a 10-GeV beam to reach the hard x-ray region. Compared with a laser undulator, a channeling radiation source comprises a small diamond chip rather than a complex laser system circulating a kilowatt of laser power.

For electrons channeling in diamond, the best available measurements are those of Azadegan [11]. A typical channeling radiation spectrum is illustrated in Figure 5. The radiation is forward directed in a cone of angle $1/\gamma$, and Doppler shifted by the factor 2γ. Including the Lorentz contraction of the crystal lattice, the photon energy scales roughly as $\gamma^{1.7}$, and spans the x-ray and gamma-ray regions. For the $1 \rightarrow 0$ transition in (110) diamond, the photon energy may be tuned from 10 to 80 keV by varying the electron energy. For a 30-MeV electron incident on a 42.5-micron thick diamond crystal, the yield on the $1 \rightarrow 0$ transition corresponds to about 0.028 photons-steradian-keV in a line 3-keV wide centered near 56 keV [11]. In conventional units, this corresponds to 10^{-9} photons-mrad^2-0.1% BW per electron.

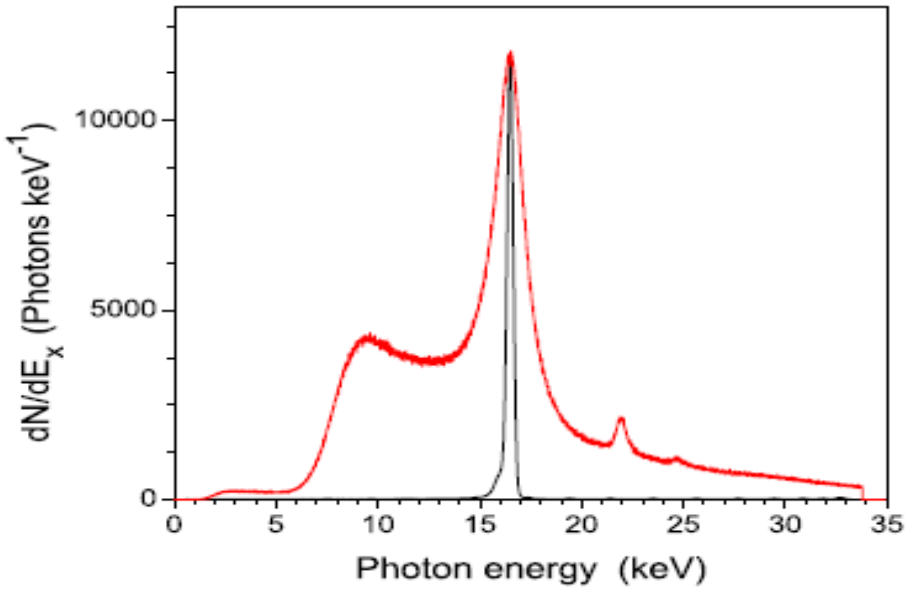

Figure 4: Observed spectrum of channeling radiation for transitions in (110) plane of diamond crystal at an electron energy of 14.6 MeV. Red: natural spectrum; black, mono-chromatized by Bragg reflection to remove the wings of the CR line and the Bremsstrahlung background. [Figure from Ref.[11]].

The spectral brilliance of the x-radiation depends on how tightly the electron beam can be focused, and this depends on the emittance of the beam. At the radiation source ELBE, in Dresden, a high-intensity channeling radiation source has been developed using a high-brightness electron beam incident on a diamond crystal [9]. Diamond is the best material for this application owing to its high thermal conductivity [12]. The normalized emittance of the beam after aperturing was 3 μm rms at an average current of 100 μA [13], which corresponds to a peak brightness on the order of 10^9 A/m^2-sterad. The beam was focused to a mm-size spot on the diamond. As much as 10^{11} photons/s were obtained in a 10% bandwidth, which corresponds roughly to an average spectral brilliance on the order of 10^6 photons/s-mm^2-mrad^2-0.1% BW.

The innovation that was proposed by the Vanderbilt group is to use a single field-emitting tip as the current source, in place of the gridded thermionic gun used at ELBE. Simulations of a single-tip field emitter yield a normalized emittance of 1.3 nm [14], which is an improvement of three orders of magnitude over the ELBE thermionic gun. In experiments at Vanderbilt, we have observed more than 10 μA average current from a single field-emitting tip [15] with brightness approaching the quantum limit [16]. The current was limited by damage to the anode, which was in close proximity. The ultimate performance of diamond tips has yet to be determined. By using a single tip it may be possible to improve the transverse brightness of the electron beam by as much as six orders of magnitude, with a corresponding improvement of the spectral brilliance of the x-ray beam. The absolute emittance of the beam from a single tip, extrapolated to 30 MeV, is ~40 pm. If we focus this at the critical angle for channeling radiation

in diamond (about 1 mrad), we get a spot diameter of 40 nm; the spectral brilliance of the x-ray beam is then 10^{12} photons/s-mm^2-mrad^2-0.1% BW at an average current of 200 nA.

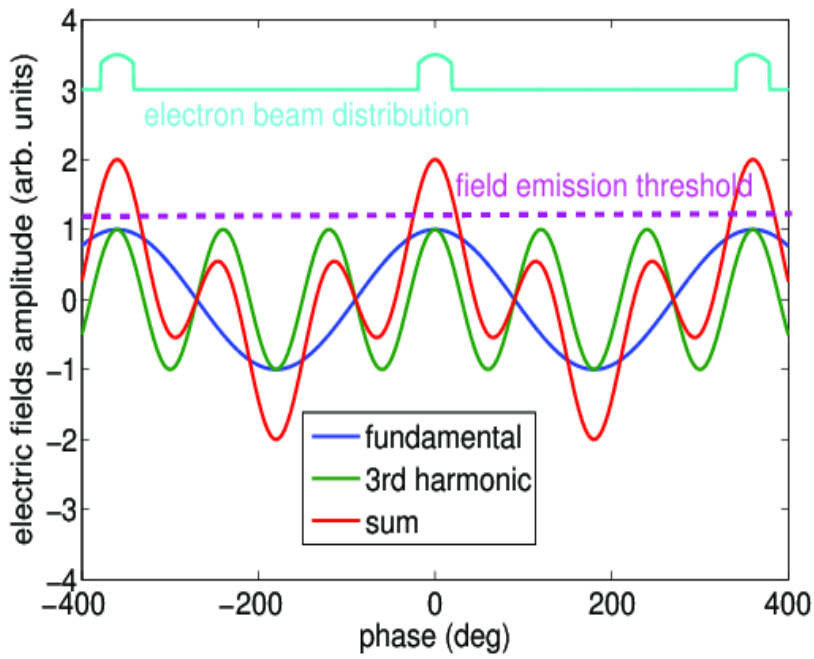

Figure 5: Two-frequency gating scheme for producing short bunch field emission cathodes.

The beam must be accelerated to high energy to create hard x-rays (~30-50 MeV). At ASTA, the first-stage acceleration will occur in the rf-gun to energies up to 4-5 MeV and further acceleration to 40 MeV will happen in CAV1 and CAV2 cavities. We currently envisioned the field-emitter cathode to be mounted on the tip of the inner conductor of a coaxial line. The coaxial line will be driven by 1.3 and 3.9-GHz signal with solid-state amplifier to bias the gate electrode and gate the field emission over duration shorter than the rf gun's fundamental frequency. Calculations indicate that such a biasing scheme will generate bunches with duration of approximately 20 ps; see Fig. 5 [17]. Preserving the exquisite emittances produced by the tip after subsequent acceleration and manipulation will be challenging. Chromatic aberrations due to energy spread in the beam, emittance dilution due to nonlinearity in the rf fields, geometric aberrations in the electron beam transport lines, and collective effects will have to be thoroughly mitigated. Since such an electron beam source represents an order-of-magnitude level increase in electron beam quality, other effects which to date have been unnoticed, may also become important. One main concern, for instance, is the extent to which Coulomb collisions at low energies (Boersch effect) will contribute to phase space dilution [18].

Because the x-rays are produced by the interaction of the electron beam with the crystal, the maximum current of the electron beam is limited by heating of, and radiation damage to, the crystal. Measurements and computations show that for diamond at room temperature the effects of heating are acceptable up to a few mA of beam current, so this will not be a limitation

even for cw operation [12]. Measurements show that radiation damage becomes significant above a total beam fluence on the order of a few C per square centimeter. Thus, the 40-nm focal spot is destroyed in about 100 μs. The crystal must be moved at about 1 mm/s, and the crystal is destroyed at the rate of 0.1 square millimeters per hour.

3.4.2 Experimental plans at ASTA

The production of channeling radiation will use the 40-MeV beam produced by ASTA; see Fig. 6. We plan to install the channeling radiation crystal downstream of a set of quadrupole magnets and just upstream of the first dipole of a chicane bunch compressor. This configuration will enable us to focus the beam on the crystal and separate the electron beam from the x-rays using the first dipole. In the straight-ahead line we plan on installing the monochromator and detector needed to characterize the x-ray radiation.

To minimize the risk, the approach will be staged. First the coaxial cathode holder will be developed and tested at the HBESL facility where the generation of field-emitted bunched beam will be demonstrated. Upon successful completion of this experiment the coaxial-line cathode holder will be installed at the ASTA. Because of the similarities between the HBESL and ASTA rf guns, we expect that the field-emitted cathode holder and associated subsystems developed during the test at HBESL will be integrally reusable without major changes. Presently, we foresee the experiment at the ASTA facility will be carried in parallel to the installation of ACC2 and ACC3 in the FY13-14 period. During this installation period only the photoinjector will be operational.

3.4.3 Other spin-off opportunities

The demonstration of the generation of bunched beam from field emission could find other applications especially since the principle could be applied to a field-emitter array cathode instead of a single-tip field emitter. The latter could produce much higher charge per bunch. For instance, if operated over the full duration of the macropulse, the total number of field-emitted bunches would be 1.3×10^6. Assuming a charge per bunch of 1 pC, this would results in a 1 mC charge within the entire macropulse. This types of unprecedented bunch format could be used to investigate high-order mode excitation in the TESLA cavity or mimic the charge per macropulse anticipated in high-intensity linacs (e.g. Project X) proposal. Alternatively a photo-field emission could be used and attosecond manipulation of the emitted bunches could be anticipated [19] thereby enabling new regimes for planned experiments such as, e.g., phase space manipulations.

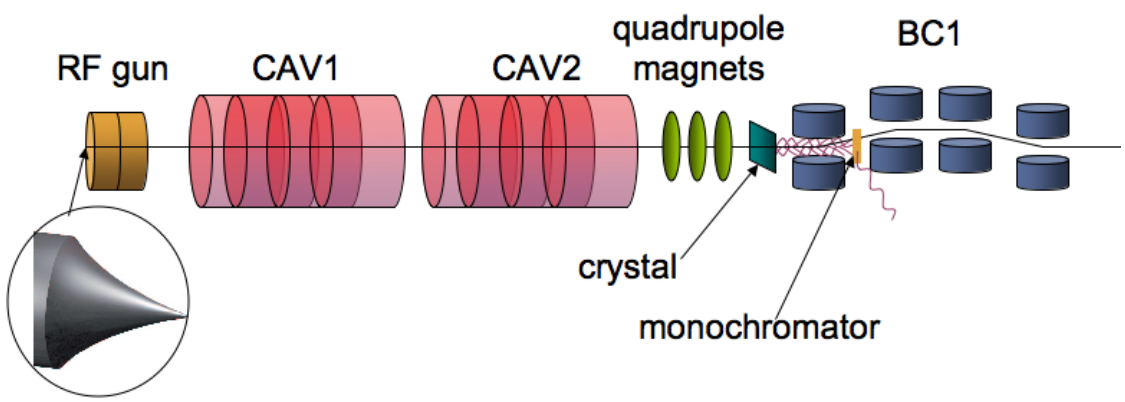

Figure 6. Layout of the X-ray channeling radiation source experiment in the 45-MeV area of ASTA.

3.5 Advanced phase space manipulations

3.5.1 Transformative applications of advanced phase space manipulations

Over the last decade, Fermilab has pioneered the experimental development of advanced phase space manipulations at the A0 photoinjector test facility. These manipulations include the generation of "flat" beams with high transverse-emittance ratio [20, 21, 22, 23] and the emittances exchange between the horizontal and longitudinal degrees of freedom [24, 25]. The beamline used for the latter experiment was also shown to be capable of producing arbitrary-shaped current profile including the production of sub-picosecond bunch trains with variable spacing as needed to produce, e.g., tunable coherent radiation [26, 27]. The combination of these two manipulations could enable the arbitrary repartitioning of emittances between the three degrees of freedom [28, 29]. Given the local expertise, this type of experiments will be resumed at ASTA with the end goal of pushing their limits to new frontiers and possibly utilizing these phase-space-manipulation concepts to advance the performances of accelerator-based light sources or new acceleration concepts.

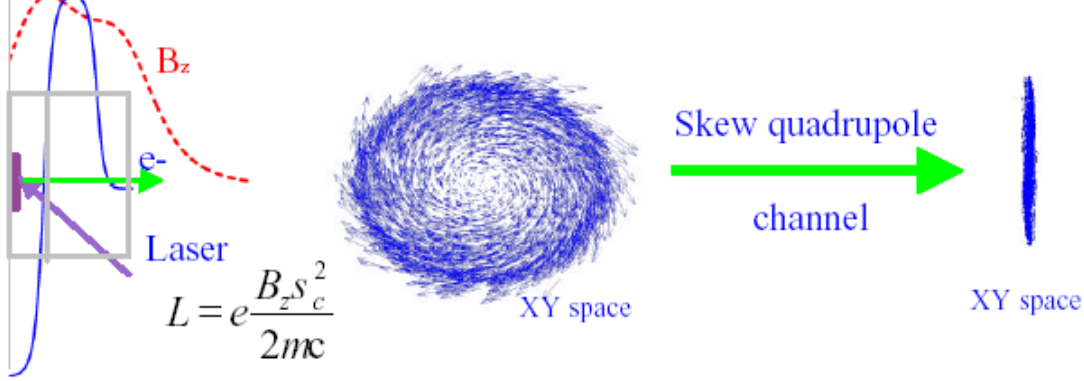

Figure 7. The round-to-flat beam transformation. The beam is produced in an rf gun (left), wherein the axial magnetic field is non-zero, thereby imparting a nonzero canonical angular momentum. Upon exit from the gun and the magnetic field, the canonical angular momentum is converted into kinetic angular momentum (middle). The angular momentum is removed by applying a torque on the beam using a system composed of three skew-quadrupole magnets. The beam is thereby made flat (right).

Under normal conditions, the electron beams generated in a photoinjector are round due to the cylindrical symmetry of the photocathode drive-laser as well as the rf acceleration and solenoidal focusing system. Several factors drive the bulk properties of an electron beam, such as space-charge, beam emittance and angular momentum. An electron beam in thermal motion inside a cathode is born into a region with an axial magnetic field ***B***, suddenly acquiring canonical angular momentum. The beam is then brought into a field-free region, and the kinetic angular momentum is removed by a set of three skew-quadrupole magnets. In this process the initially equal emittances are partitioned into unequal emittances ($\gamma\varepsilon_+$, $\gamma\varepsilon_-$), preserving the product: $\gamma\varepsilon_x \times \gamma\varepsilon_y = \gamma\varepsilon_+ \times \gamma\varepsilon_-$; see Figure 3.

An unequal partitioning of equal emittances is not possible in a symplectic process; in a symplectic process the emittances in different directions can either remain the same or be exchanged among themselves. The flat-beam technique circumvents this limitation because the process of beam birth in a magnetic field is non-symplectic. The expected flat beam transverse emittances are [30]:

$$\gamma\varepsilon_\pm = \left[(\gamma\varepsilon)^2 + (\gamma\Lambda)^2\right]^{1/2} \pm \gamma\Lambda \xrightarrow{\gamma\Lambda >> \gamma\varepsilon} \begin{cases} 2\gamma\Lambda \\ \dfrac{\gamma\varepsilon}{2\Lambda\gamma} \end{cases}$$

where Λ is related to the beam's mean canonical angular momentum. The emittance ratio after the round-to-flat-beam transformation is given by

$$\frac{\varepsilon_+}{\varepsilon_-} \approx \left(\frac{2\gamma\Lambda}{\gamma\varepsilon}\right)^2 = \left(\frac{eB(\sigma_c)^2}{mc\gamma\varepsilon}\right)^2 >> 1,$$

where e is the electron charge, m is the electron mass, c is the speed of light, and σ_c is the transverse rms beam size of the laser on the photocathode.

The flat-beam technique was experimentally demonstrated at Fermilab's A0 Photoinjector [23] where an emittance ratio of ~100 was achieved; see Fig. 8.

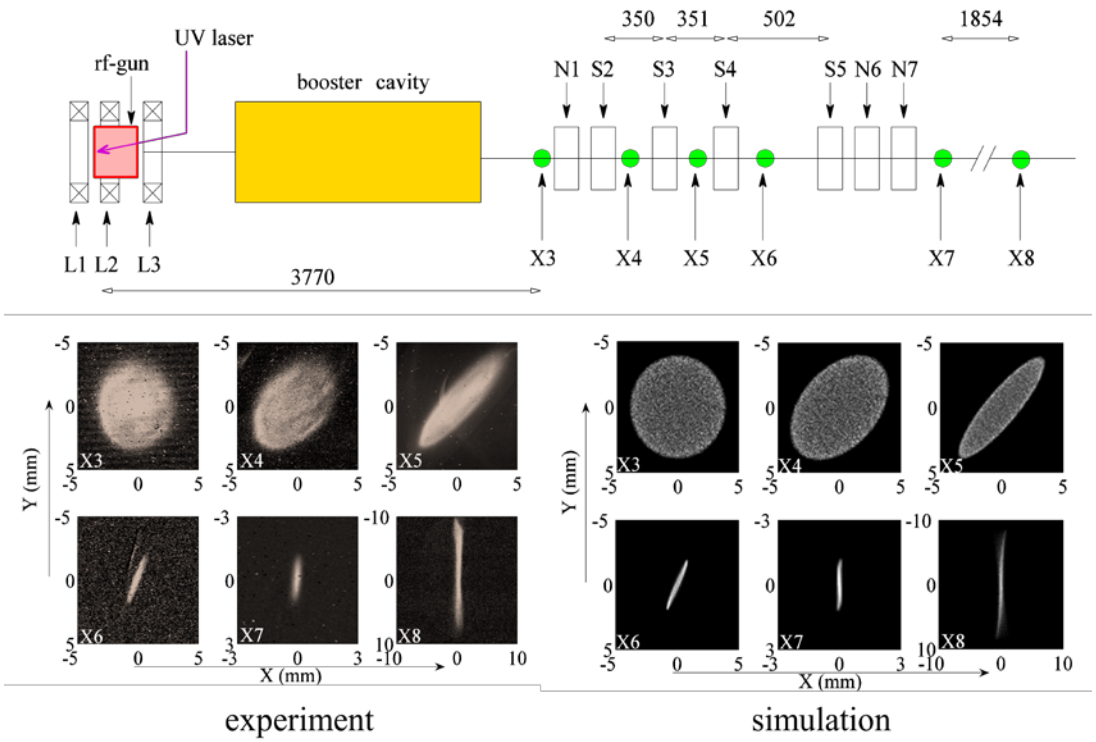

Figure 8: The round-to-flat beam transformation experiment at A0 photoinjector (from Ref.[22]). Top: experimental configuration (the labels "X", "N", "S" respectively represent the locations of diagnostics, normal and skew quadrupole magnets). Bottom: transverse measured (left) and simulated (right) beam density at different axial locations along the accelerator beamline.

The ASTA photoinjector incorporates a set of three skew-quadrupole magnets, a round-to-flat-beam transformer (RFBT), to possibly convert an incoming magnetized round beam into a flat beam. Furthermore, the solenoidal lenses surrounding the rf gun can be axially moved. The bucking solenoid on the rf-gun was designed to provide a large axial field on the photocathode surface. Therefore, by properly positioning the solenoidal lenses and setting their currents, the axial magnetic field on the photocathode can be tuned from zero to thousands of Gauss. At bunch charge of 1.0 nC and beam energy of 40 MeV, the normalized emittance is optimized around $\varepsilon_{\perp}^{n}$ =2.3 μm [4]. This includes the thermal emittance which is about 0.85 μm for a residual kinetic energy of 0.55 eV from CsTe cathode. Considering the case of a 1000-G axial magnetic field on the photocathode would result in a normalized angular momentum γL= 29.64 μm; then the achievable flat-beam transverse normalized emittances partition is $(\gamma\varepsilon_{-},\gamma\varepsilon_{+})\approx$ (0.1, 59.4) μm corresponding to an emittance ratio of ~600. The small emittance will be challenging to measure with the standard multislit method but should be properly diagnosed

with the quadrupole scan method. Accelerating these flat beams to 250 MeV while preserving the small emittance will also present interesting challenges and remains to be demonstrated.

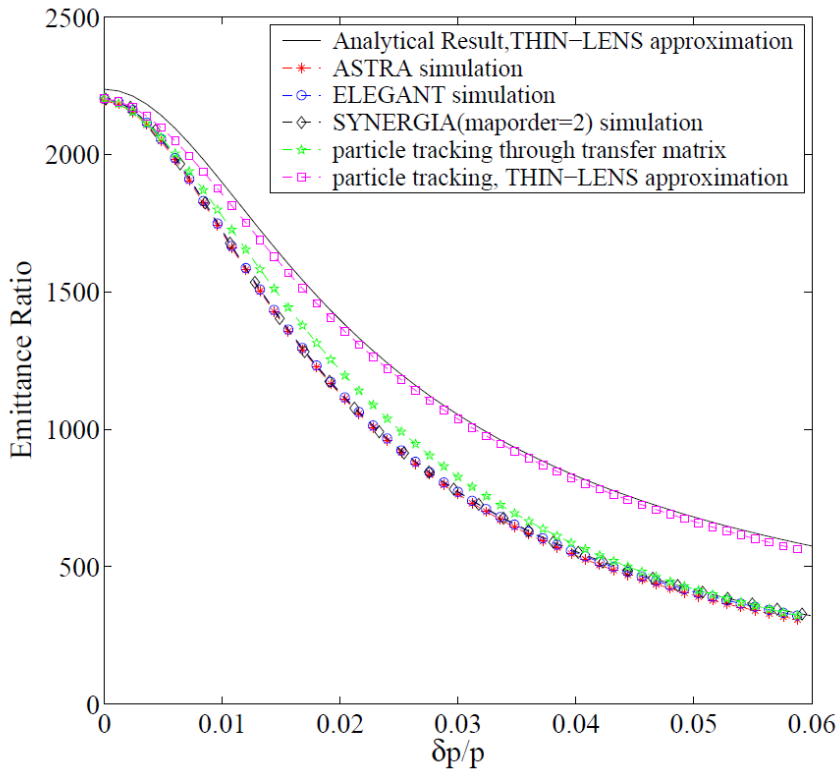

Figure 9: The Impact of chromatic aberrations on the RFTB insertion.

Finally, compressing the produced flat beam could provide exciting opportunities: compressed flat beam can be used for image charge undulators. In addition, flat beams could also provide a way to mitigate deleterious effects in magnetic chicane bunch compressor. A full compression in the injector bunch compressor (BC1) requires the longitudinal phase space to be chirped with a chirp given by $\frac{\partial\delta}{\partial z} = -\frac{1}{R_{56}}$ where $R_{56} \approx -0.2$ m is the momentum compaction associated to BC1. Therefore the required chirp will only be $\partial\delta/\partial z \approx 5\,\mathrm{m}^{-1}$ corresponding to a rms relative momentum spread of $\sigma_\delta \approx \sigma_z(\partial\delta/\partial z) \le 1\%$ for typical bunch length expected downstream of the 2nd accelerating cavity (CAV2). This fractional energy spread value should results in manageable chromatic aberrations in the round-to-flat beam transformer that should not significantly deteriorate the emittance ratio; see Fig. 9. This would be a significant improvement over the flat beam experiment carried at the A0 photoinjector where the low momentum compaction imposed large energy spread.

3.5.3 Transverse-to-longitudinal phase space exchange

The transverse and longitudinal phase space coordinate can be exchanged by a beamline composed of a deflecting cavity operating on the TM_{110} flanked by two dispersive sections. A

simple implementation of such a beamline is the "double-dogleg configuration" where two dispersive sections are simple doglegs composed of two dipoles; see Fig. 10.

In such a configuration the condition for phase space exchange is that the normalized deflecting strength of the cavity satisfies $\kappa = -1/\eta$. When this condition is fulfilled and under the thin lens approximation, the horizontal and longitudinal phase space coordinates (x,x',z,δ) before and after the EEX are related via the transfer matrix of the double dogleg beamline as follows:

$$\begin{pmatrix} x \\ x' \\ z \\ \delta \end{pmatrix}_{out} = \begin{pmatrix} 0 & 0 & \frac{L+S}{\alpha L} & \alpha S \\ 0 & 0 & \frac{1}{\alpha L} & \alpha \\ \alpha & \alpha S & 0 & 0 \\ \frac{1}{\alpha L} & \frac{L+S}{\alpha L} & 0 & 0 \end{pmatrix} \begin{pmatrix} x \\ x' \\ z \\ \delta \end{pmatrix}_{in}$$

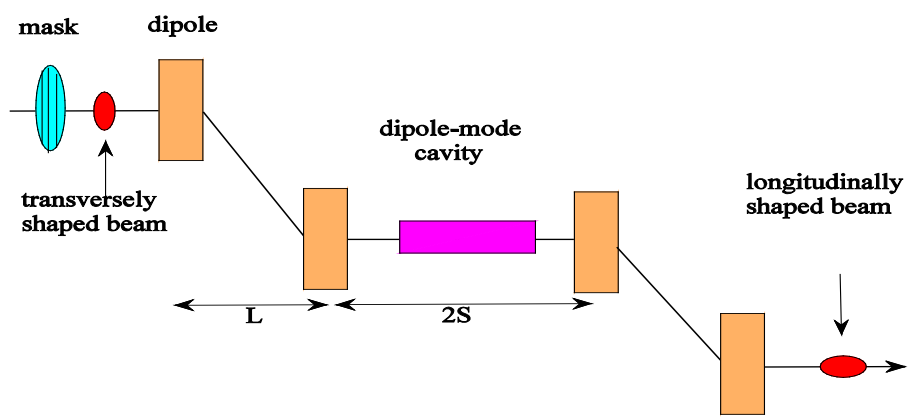

Figure 10: The Impact of chromatic aberrations on the RFTB insertion.

Since this beamline exchanges the phase space coordinates, it also swaps the transverse and horizontal emittances. In fact this was the initial motivation for developing such types of beamline [31]. A proof-of-principle experiment demonstrating the exchange of transverse and longitudinal emittances was carried at the A0 photoinjector [25]. It was later realized that this phase space exchange beamline could also be used as current shaper [32] and proof-of-principle experiment was carried at the A0 photoinjector; see Fig. 11. A byproduct of this experiment was the generation of narrowband THz coherent transition radiation. The radiation was shown to have a 20-25 % FWHM relative bandwidth and was tunable over the 0.4-0.9 THz range. These experiments were limited by the mask used to produce a transversely-segmented beam (the mask was indeed optimized to measure the beam emittance). At the A0

photoinjector, the deflecting cavity used was a LN-cooled normal conducting cavity composed of five elliptical cells following the design of a superconducting cavity developed for kaon separation [33].

We plan on continuing phase space exchange experiments at ASTA. Several avenues to improve over the series of experiments performed at the A0 photoinjector are under consideration. The overaching goals of this "second generation" phase space exchange experiments are

1. to improve the performance of the first generation phase space exchange experiment, and
2. to find beamline configuration that would be more practical.

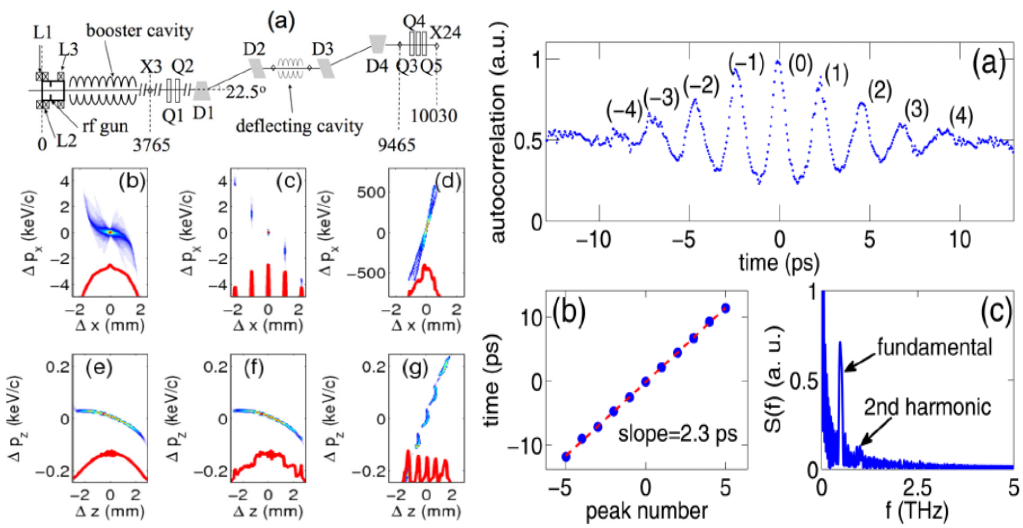

Figure 11: Left figures: (a) experimental configuration and simulated transverse (b,c,d) and longitudinal (e,f,g) phase spaces before (b,e) and after (c,f) the multi-slit mask and downstream (d,g) of the emittance-exchanger beamline. Right figure: typical autocorrelation of transition radiation (a) and corresponding peak separation (b) and frequency analysis (c).

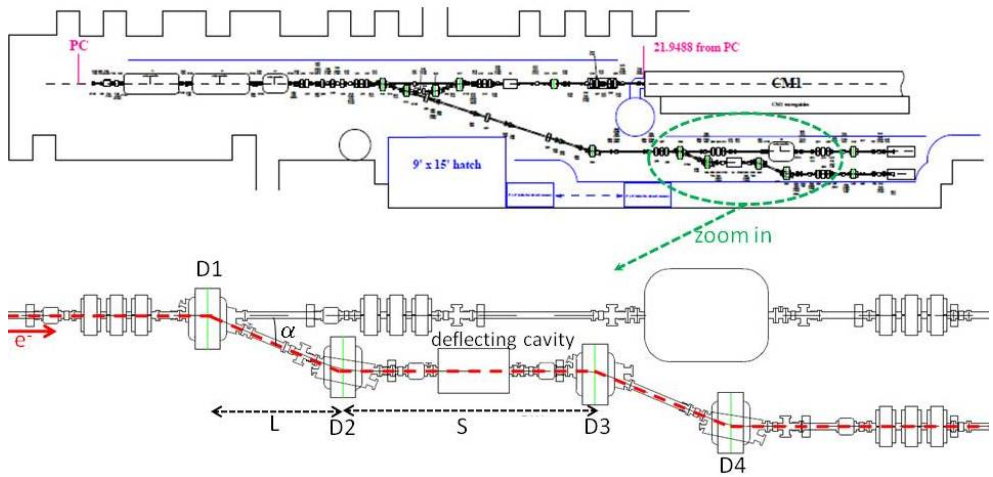

Figure 12: The NML injector and double dogleg beamline for transverse-to-longitudinal phase space exchange

Item (1) consists in improving the diagnostics downstream of the phase space exchanger beamline (the A0 experiment did not have any viable longitudinal phase space diagnostics which precluded a direct measurement of the final longitudinal emittance) and possibly considering an "hybrid" deflecting cavity that will also have a 6th cell operating on the TM_{010} mode. The latter improvement was shown to cancel some aberration associated the realistic (and not thin lens model) of deflecting cavities [34]. The current 3.9-GHz rf system should be able to drive such an hybrid cavity provided the dispersion at the cavity is close to 0.8 m (for a 40-MeV beam); see Fig. 13. One option would consist in installing a double-dogleg beamline in the 40-MeV experimental area; see Fig. 12. However due to the limited 3.9-GHz klystron power (80 kW), the use of a LN-cooled deflecting cavity forces us to increase the dispersion in order to lessen the deflecting strength required for full phase space exchange. In current layout, the dipole magnets in each dogleg are separated by 1.07m and the distance between the two center dipole is 1.99 m. Each dipole bends the beam by 22.5° while each dogleg generates a dispersion of 44 cm. The beamline was modeled using General Particle Tracer with 3D space-charge effects included for a 250 pC and 40 MeV electron bunch. The design is in essence very similar to the setup used at the A0 photoinjector but would include better diagnostics. In addition it could support experiment aiming at repartioning the emittances within the three degrees of freedom. In such experiments, the flat beam transform would be used to create a flat incoming beam and the phase space exchange would exchange the horizontal and longitudinal emittances. This versatility would allow for parametric studies of the phase space exchange mechanism. Finally the beamline could also support more advanced current shaping technique. Using triangular mask (or shaping the transverse profile of the laser on the photocathode) could be used to produce ramped bunches which have extremely important applications in beam driven wakefield acceleration technique as they enhance the transformer ratio.

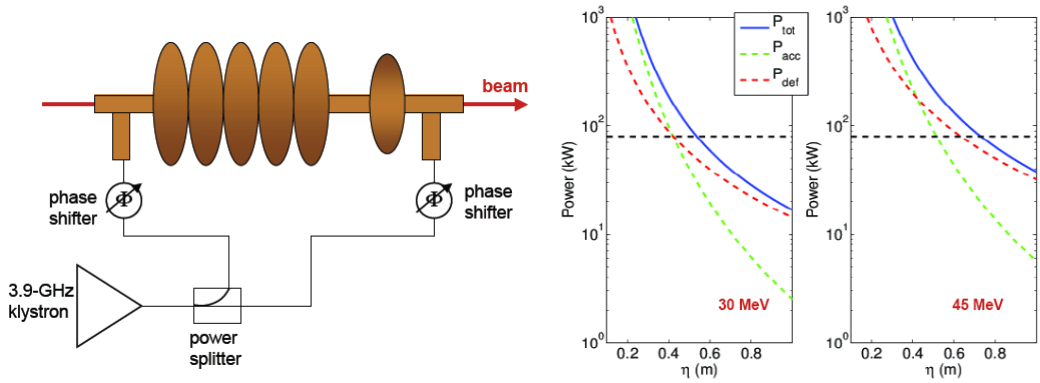

Figure 13: The "thin-lens" deflecting cavity consisting of a five-cell TM110 cavity followed by a single-cell TM010 cavity (left). Requirements on klystron power for ideal longitudinal to transverse phase space exchange as a function of the dispersion value at the cavity location. The calculations are performed for a 3.9-GHz klystron feeding an LN-cooled system. The horizontal black line corresponds to the maximum power available from the available klystron.

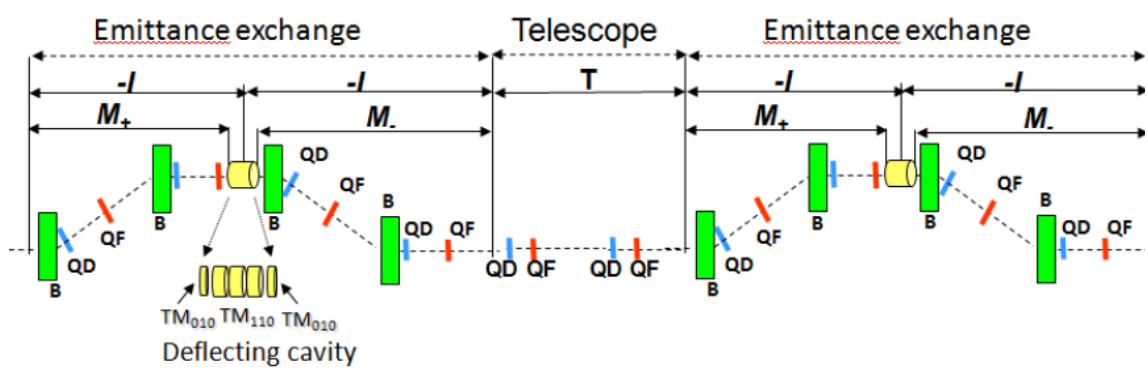

Figure 14. A possible configuration for a double phase space exchange [from Ref. [34]].

Beside the double-dogleg beamline, other configurations are also possible, such as the magnetic chicane with quadrupoles inserted between the dipole. This latter setup has the main advantage of not translating the beam direction and could be a more suitable configuration for a higher energy phase space exchanger. It could also open the exploration of trade off between dispersion and deflecting strength. Numerical simulations are currently underway to explore possible layouts at ASTA.

3.5.4 Transverse-to-longitudinal phase space exchange at ~700 MeV

The chicane-type configuration described in the previous section could form the basis for a phase space exchange beamline downstream of the accelerating section. It was recently suggested by A. Zholents that using two phase space exchangers back to back separated by an appropriate optical lattice could be used to perform the current shaping described above; see Fig. 14. The shaper would be located between the two emittance exchangers.

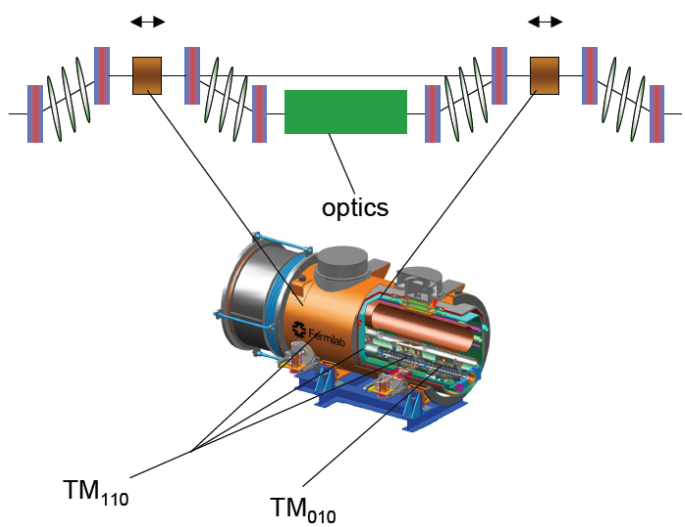

Figure 15. A possible configuration for a 3.9 GHz deflecting/accelerating hybrid SCRF structure for a double phase space exchanger in the high energy beamline of ASTA

The overall advantage of such a "double phase space exchanger" configuration compared to a single phase space exchanger is that it lets the transverse emittances untouched (under linear optics). Another important application of the double phase space exchanger scheme is to compress the beam without requiring an incoming energy correlation along the bunch. This is achieved by inserting a telescope between the two phase space exchanger, thus a bunch can be compressed without energy chirp as needed in a conventional chicane-type bunch compressor. Therefore the beam can be impressed after it goes through all the acceleration sections, thus avoid the collective effects associated with high peak current in the linac. The new double EEX bunch compressor can also be used for frequency up-conversion of the energy modulation provide by the laser interaction with electron beam, thus can possibly seeding a free-electron laser at a significantly higher harmonics; or it can also be used to do frequency down-conversion for generation of THz radiation.

The design of such a double EEX beamline would require a detailed study. From first order-of-magnitude analysis, LN_2-cooled cavities would put a high demands (several MW) on the klystrons. Thus it is natural to consider a SCRF system operating at 3.9 GHz similar to the system developed at Fermilab for kaon separation and longitudinal phase space linearization of the FLASH accelerator at DESY. A possible configuration is diagrammed in Fig. 15.

3.6 Integrable-optics test accelerator (IOTA) ring construction and operation

3.6.1 Introduction

What prevents us from building super-high intensity accelerators? The answer is case-specific, but it often points to one of the following phenomena: machine resonances, various tune shifts (and spreads), and instabilities. These three phenomena are interdependent in all present machines, which are built to have "linear" focusing optics (also called lattice). A path towards alleviating these phenomena can be opened by making accelerators nonlinear. This idea is not totally new: Orlov (1963) and McMillan (1967) have proposed initial ideas on nonlinear focusing systems for accelerators. However, practical implementations of such ideas proved elusive, until recently when Danilov and Nagaitsev proposed a solution for nonlinear integrable accelerator lattice that can be implemented with special magnets [35]. In this document we propose a proof-of-principle experiment for demonstration of the concept, and describe the design of machine for this demonstration – the Integrable Optics Test Accelerator (IOTA).

3.6.2 Concept of nonlinear integrable optics

3.6.2.1 Nonlinear Integrable Optics and Potential

Lattice design of all present accelerators incorporates dipole magnets to bend particle trajectory and quadrupoles to keep particles stable around the reference orbit. These are "linear" elements because the transverse force is proportional to the particle displacement, *x* and *y*. This linearity results (after the action-phase variable transformation) in a Hamiltonian of the following type:

$$H(J_1, J_2) = \nu_x J_1 + \nu_y J_2, \tag{1}$$

where ν_x and ν_y are betatron tunes and J_1 and J_2 are actions. This is an integrable Hamiltonian. The drawback of this Hamiltonian is that the betatron tunes are constant for all particles regardless of their action values. It has been known since early 1960-s that the spread of betatron tunes is extremely beneficial for beam stability due to the so-called Landau damping. However, because the Hamiltonian (1) is linear, any attempt to add non-linear elements (sextupoles, octupoles) to the accelerator generally results in a reduction of its dynamic aperture, resonant behavior and particle loss. A breakthrough in understanding of stability of Hamiltonian systems, close to integrable, was made by Nekhoroshev [36]. He considered a perturbed Hamiltonian system:

$$H = h(J_1, J_2) + \varepsilon q(J_1, J_2, \theta_1, \theta_2), \tag{2}$$

where *h* and *q* are analytic functions and ε is a small perturbation parameter. He proved that under certain conditions on the function *h*, the perturbed system (2) remains stable for an exponentially long time. Functions *h* satisfying such conditions are called *steep* functions with quasi-convex and convex being the steepest. In general, the determination of steepness is quite complex. One example of a non-steep function is a linear Hamiltonian Eq. (1).

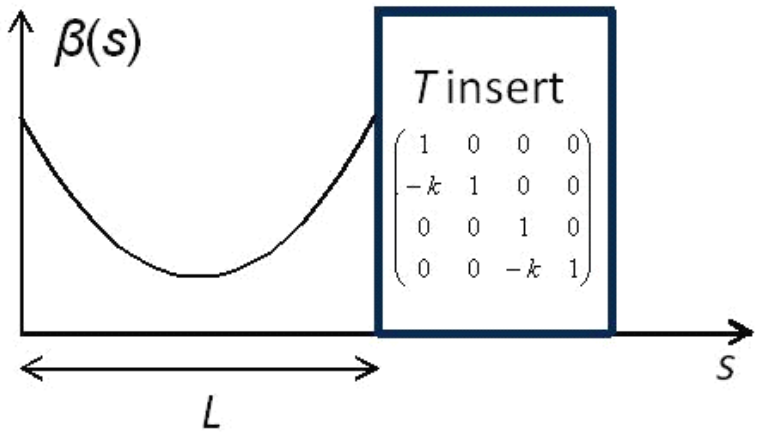

Figure 16. An element of periodicity: a drift space with equal beta-functions followed by a *T*-insert.

In Ref. [35] three examples of nonlinear accelerator lattices were proposed. Here we will concentrate on one of the lattices, which results in a steep (convex) Hamiltonian.

Consider an element of lattice periodicity consisting of two parts: (1) a drift space, *L*, with exactly equal horizontal and vertical beta-functions, followed by (2) an optics insert, *T*, which is comprised of linear elements and has the transfer matrix of a thin axially symmetric lens; see Figure 16.

Let us now introduce additional transverse magnetic field along the drift space *L.* The potential, $V(x, y, s)$, associated with this field satisfies the Laplace equation, $\Delta V = 0$.

Now we will make a normalized-variable substitution [35] to obtain the following Hamiltonian for a particle moving in the drift space *L* with an additional potential *V*:

$$H_N = \frac{p_{xN}^2 + p_{yN}^2}{2} + \frac{x_N^2 + y_N^2}{2} + U\left(x_N, y_N, \psi\right), \tag{3}$$

where

$$U\left(x_N, y_N, \psi\right) = \beta(\psi) V\left(x_N \sqrt{\beta(\psi)}, y_N \sqrt{\beta(\psi)}, s(\psi)\right) , \tag{4}$$

and ψ is the "new time" variable defined as the betatron phase,

$$\psi' = \frac{1}{\beta(s)} . \tag{5}$$

The potential *U* in equation (3) can be chosen such that it is time-independent [1]. This results in a time-independent Hamiltonian (3). We will now choose a potential such that the Hamiltonian (3) possesses the second integral of motion. We will omit the subscript *N* from now on.

Consider potentials [3[37]] that can be presented in elliptic coordinates in the following way

$$U(x,y)=\frac{f(\xi)+g(\eta)}{\xi^2-\eta^2}, \tag{6}$$

where *f* and *g* are arbitrary functions,

$$\xi=\frac{\sqrt{(x+c)^2+y^2}+\sqrt{(x-c)^2+y^2}}{2c} \quad \eta=\frac{\sqrt{(x+c)^2+y^2}-\sqrt{(x-c)^2+y^2}}{2c} \tag{7}$$

are elliptic variables and *c* is an arbitrary constant.

The second integral of motion yields

$$I\left(x,y,p_x,p_y\right)=\left(xp_y-yp_x\right)^2+c^2p_x^2+2c^2\frac{f(\xi)\eta^2+g(\eta)\xi^2}{\xi^2-\eta^2} \tag{8}$$

First, we would notice that the harmonic oscillator potential ($x^2 + y^2$) can be presented in the form of Eq. (6) with $f_1(\xi)=c^2\xi^2\left(\xi^2-1\right)$ and $g_1(\eta)=c^2\eta^2\left(1-\eta^2\right)$. Second, we have found the following family of potentials that satisfy the Laplace equation and, at the same time, can be presented in the form of Eq. (6):

$$f_2(\xi)=\xi\sqrt{\xi^2-1}\left(d+t\,\mathrm{acosh}\left(\xi\right)\right) \quad g_2(\eta)=\eta\sqrt{1-\eta^2}\left(q+t\,\mathrm{acos}\left(\eta\right)\right), \tag{9}$$

where *d*, *q*, and *t* are arbitrary constants. Thus, the total potential energy in Hamiltonian (3) is given by

$$U(x,y)=\frac{x^2}{2}+\frac{y^2}{2}+\frac{f_2(\xi)+g_2(\eta)}{\xi^2-\eta^2}. \tag{10}$$

Of a particular interest is the potential with *d* = 0 and $q=\frac{\pi}{2}t$, because its lowest multipole expansion term is a quadrupole. Figure 17 presents a contour plot of the potential energy Eq. (10) for *c* = 1 and *t* = 0.4.

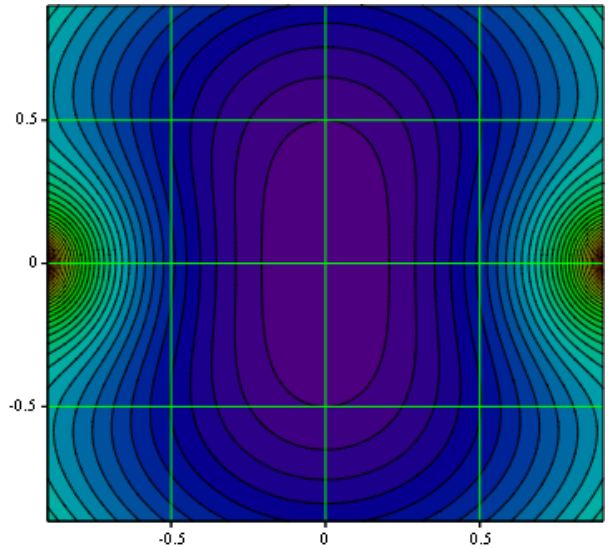

Figure 17: Contour plot of the potential energy Eq. (10) with *c* = 1 and *t* = 0.4. The repulsive singularities are located at x = ±c and y = 0

The multipole expansion of this potential for *c* = 1 is as follows:

$$U(x,y) \approx \frac{x^2}{2} + \frac{y^2}{2} + t\,\mathrm{Re}\left((x+iy)^2 + \frac{2}{3}(x+iy)^4 + \frac{8}{15}(x+iy)^6 + \frac{16}{35}(x+iy)^8 + \ldots \right) \tag{11}$$

where *t* is the magnitude of the nonlinear potential.

Since the 2D Hamiltonian with this potential has two analytic integrals of motion, it is integrable and thus can be expressed as an analytic function of actions:

$$H = h(J_1, J_2), \tag{12}$$

where

$$J_1 = \frac{1}{2\pi}\oint p_\eta d\eta \quad J_2 = \frac{1}{2\pi}\oint p_\xi d\xi \tag{13}$$

3.6.2.2 Maximum nonlinear tune shift

The potential (10) provides additional focusing in *x* for *t* > 0 and defocusing in *y*. Thus, for a small-amplitude motion to be stable, one needs 0 < *t* < 0.5. This corresponds to the following small-amplitude betatron frequencies,

$$\nu_1 = \nu_0 \sqrt{1+2t} \quad \nu_2 = \nu_0 \sqrt{1-2t} \quad , \tag{14}$$

where ν_0 is the unperturbed linear-motion betatron frequency. For arbitrary amplitudes the frequencies are obtained by

$$\nu_1(J_1, J_2) = \frac{\partial h}{\partial J_1} \quad \nu_2(J_1, J_2) = \frac{\partial h}{\partial J_2} \quad . \tag{15}$$

Figure 18 presents frequencies $\nu_1(J_1, 0)$ and $\nu_2(0, J_2)$, normalized by ν_0 for t = 0.4.

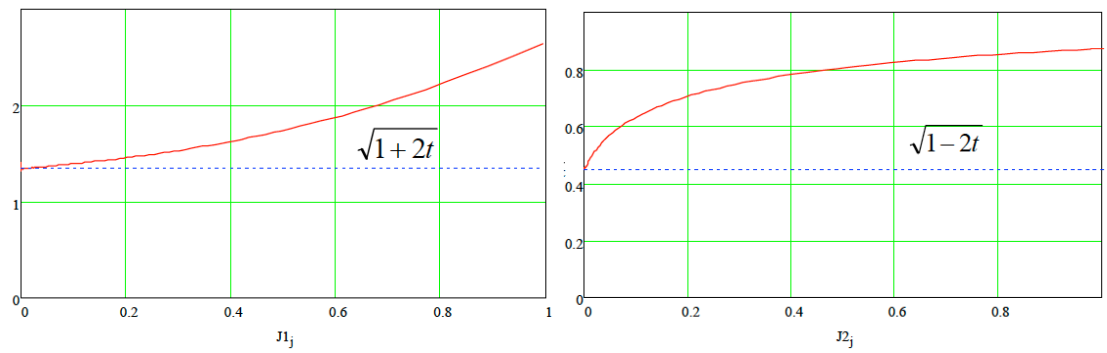

Figure 18: Betatron oscillation frequencies of the two modes - 1 (left) and 2 (right) normalized by ν_0 as functions of actions. Nonlinearity strength parameter t = 0.4.

The unperturbed linear motion tune ν_0 - the betatron phase advance over the drift space L, is limited to 0.5 (in units of 2π). The phase advance in T-insert must be a multiple of 0.5. This makes the full tune of one element of periodicity 0.5+0.5n. Thus, the theoretical maximum attainable nonlinear tune shift per cell is ~0.5 for mode 1 and ~0.25 for mode 2. Expressed in terms of the full betatron tune per cell, this tune shift can reach 50% (0.5/(0.5+0.5)).

Numerical simulations with single and multi particle tracking codes were carried out in order to determine the tune spread that can be achieved in a machine built according to the above recipe [38,39,40]. Various imperfections were taken into account, such as the perturbations of T-insert lattice, synchrotron oscillations, and other machine nonlinearities. In Figure 19 a result of one of the simulations is presented. The tune footprint obtained with Frequency Map Analysis [41] demonstrates that vertical tune spread exceeding 1 can be achieved and very little resonances are caused by imperfections. No dynamic aperture was observed in the system.

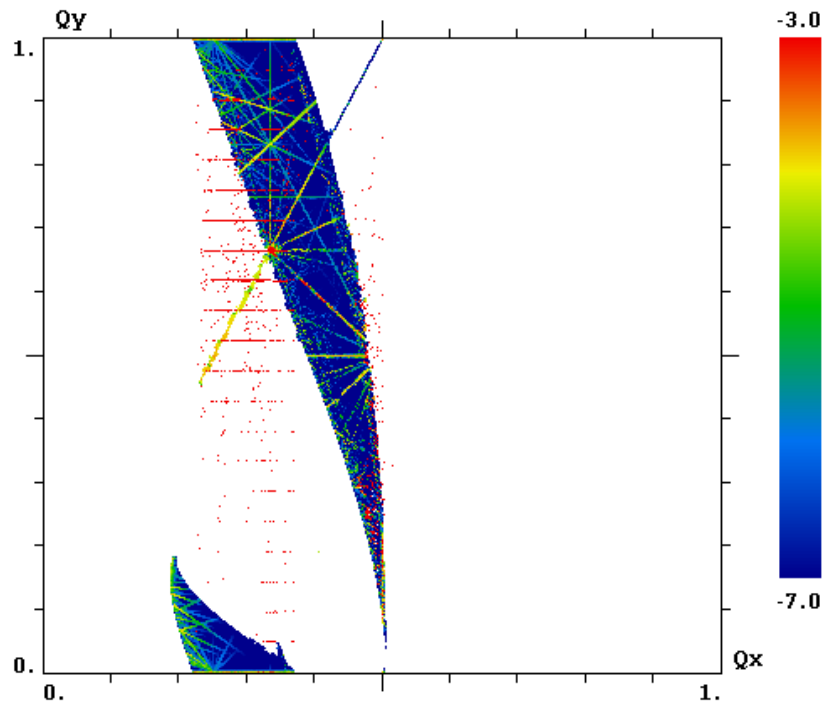

Figure 19: Beam tune footprint for ν_0 = 0.3, four elements of periodicity, *t* = 0.4. Simulation with Lifetrac Frequency Map Analysis.

3.6.3 IOTA goals and scope

In Section 2 we demonstrated that using conventional and special nonlinear focusing magnets it is possible to construct an accelerator lattice, in which the betatron motion is strongly nonlinear yet stable. The strong nonlinearity of betatron motion would result in a significant spread of betatron tunes of particles within the bunch (up to 50% of the nominal tune), thus providing strong Landau damping of coherent instabilities.

The superconducting RF test facility at Fermilab (formerly NML) will provide electron beam with energies up to 750 MeV. The experimental area at the end of the linac will be located in a 20×15 m hall, which is large enough to house a small electron storage ring.

We propose to construct the Integrable Optics Test Accelerator (IOTA) ring, which would use the beam from the NML 1.3 GHz SRF linac with the goal of *demonstration of the possibility to achieve very large nonlinear tune shifts in a realistic accelerator design*. This proof-of principle experiment would *only concentrate on the single-particle motion stability in the nonlinear integrable system*, leaving the studies of collective effects and attainment of high beam current to future research.

Research at IOTA will include experiments on the following topics:

- Achievement of large nonlinear tune shift/spread without degradation of dynamic aperture
- Suppression of strong lattice resonances (e.g. by crossing the integer resonance by part of the beam without intensity loss)
- Stability of nonlinear system to perturbations: chromatic effects, effect of synchrotron oscillations, lattice distortions
- Studies of different variants of nonlinear magnet design

In addition to the primary goal, the ring can accommodate other Advanced Accelerator R&D experiments and/or users. This is possible because only a portion of the ring circumference will be occupied with nonlinear magnets and otherwise the machine is a conventional low-energy storage ring. One of the AARD experiments incorporated in the current design of the ring is the Optical Stochastic Cooling.

3.6.4 IOTA Design

3.6.4.1 Machine Lattice

The machine lattice must satisfy the following design criteria:

- Be periodic, with the element of periodicity comprised of a drift space with equal beta-functions, and a focusing and bending block with the betatron phase advance in both planes equal to π (T-insert in Fig. 1).
- The drift space must be long enough to accommodate practical nonlinear magnets. We set the minimum drift length to 2 m.
- The T-insert must be tunable to allow a wide range of phase advances (and beta-functions) in the drift space in order to study different betatron tune working points.
- It is preferable that the focusing block is achromatic in order to avoid strong coupling between the transverse and longitudinal degrees of freedom.
- The ring must have one long (5 m) straight section for the Optical Stochastic Cooling experiment.
- The machine must fit in the footprint of the experimental hall and be properly oriented with respect to the injection line.

In our design the ring is made of four cells. The cells are mirror-symmetric in pairs, and each consists of 8 quadrupoles and two dipole magnets bending by 30 and 60 degrees. With the betatron phase advance per cell of 0.8, this makes the total betatron tune of 3.2. Hence, in the extreme case the maximum tune shift generated by the nonlinear magnets may reach 1.6, meaning some particles in the bunch will cross an integer resonance.

This design provides 2 m insertions for the nonlinear magnets, two 1 m long straight sections for RF and other systems, and two 5 m sections – one for injection/extraction and one for Optical Stochastic Cooling setup. The minimal number of quadrupole magnets required to implement an axially symmetric lens in a straight section is five. The large

number of quadrupoles we use permits a wide range of tuning for the betatron tune, which can be varied between 2.4 and 3.6, and dispersion and momentum compaction.

Table 1 lists the main parameters of the machine. Figures 20,21 show the machine layout in the experimental hall, and lattice functions of one cell.

Table 2: IOTA Parameters

Parameter	Value	Unit
Beam Energy	150	MeV
Circumference	30.4	m
Bending dipole field	0.5	T
RF voltage	50	kV
Maximum β–function	22	m
Momentum compaction	0.14	
Betatron tune	Q_x, Q_y=3.2 (2.4 to 3.6)	
Equilibrium transverse emittance r.m.s.	0.06	μ m (non-normalized)
Synchrotron radiation damping time	1.0	sec(~10^7 turns)

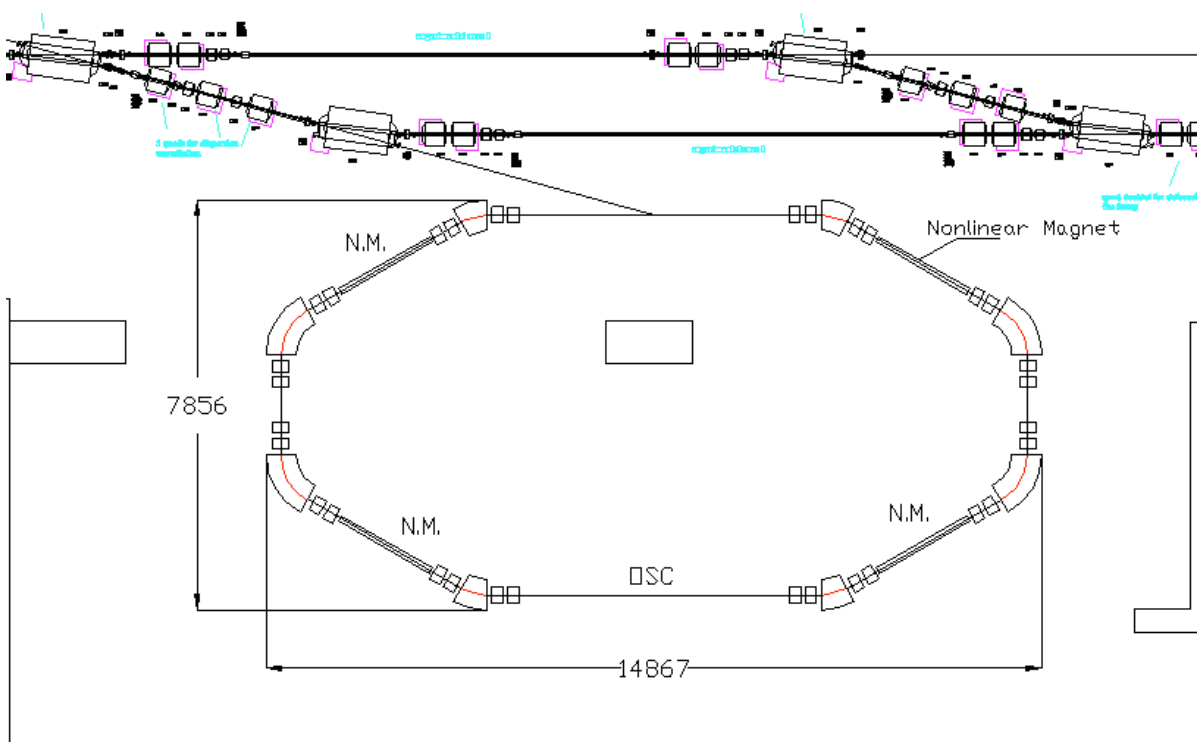

Figure 20: IOTA ring layout.

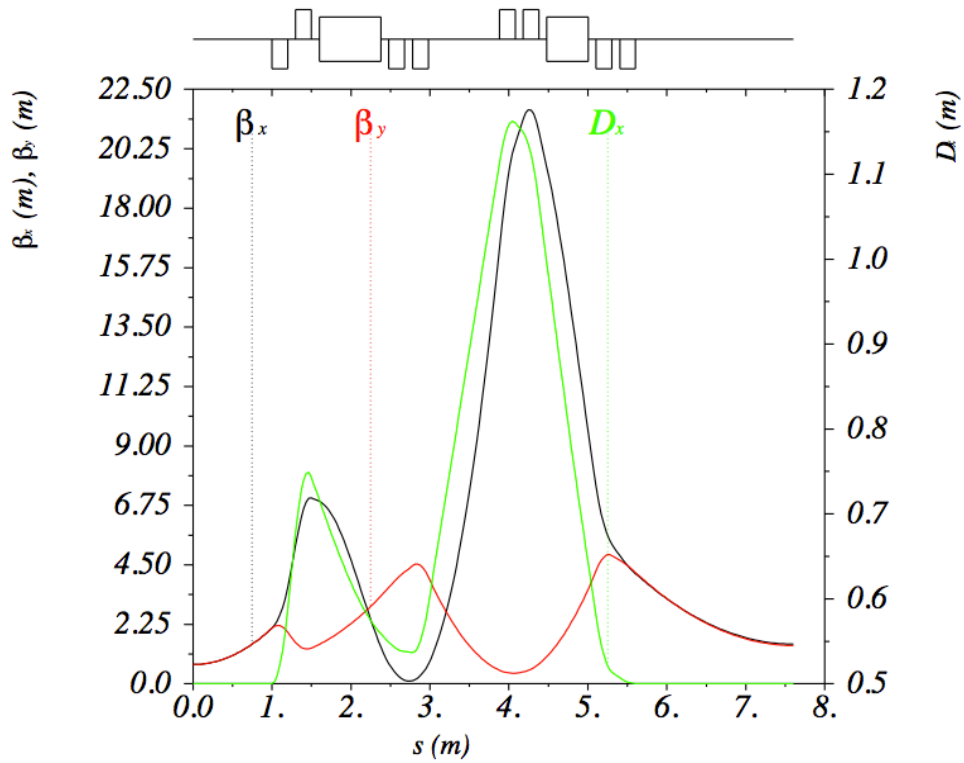

Figure 21: Lattice functions of the element of periodicity.

3.6.4.2 Nonlinear Magnets

The condition of the Hamiltonian time-independence requires that the nonlinear potential must *continuously* change along the length of the nonlinear section (Eq. 4). The potential is defined by two parameters: the strength parameter *t*, and the geometric parameter *c*, which represents the distance between the singularities, or the element aperture (Eq. 10). The geometric parameter *c* scales as the square root of β-function in the nonlinear straight section, and the strength parameter *t* scales as $1/\beta$. Since it's not practical to manufacture a magnet with complex varying aperture, we consider approximating the continuously varying potential with a number of thin magnets of constant aperture. Figure 22 shows the distribution of strength of the lowest (quadrupole) harmonic in 20 thin magnets.

The magnetic potential can be expanded into multipole series Eq. (11). However, this expansion is only valid inside the $r = \sqrt{x^2 + y^2} < c$ circle. Vertical oscillation amplitudes $y > c$ are essential for achievement of large tune spread. By proper shaping of the magnetic poles we were able to achieve good field quality in the region $x < c$, $y < 2{\times}c$ (Fig. 23). The magnet can be optimized further to include fringe-field effects and extend the good field region.

In order to demonstrate the high tune spread within the beam, the transverse beam size must be comparable to the distance between the poles of the magnet. For the chosen ring energy and equilibrium emittance, the beam size σ_x, $\sigma_y \approx 0.25$ mm, which would require impractically small transverse dimensions of the nonlinear elements. However, due to the very long damping time it is possible to "paint" a larger area with the small emittance linac beam. Hence, we considered nonlinear elements with the aperture $2\times c \approx 2$ cm.

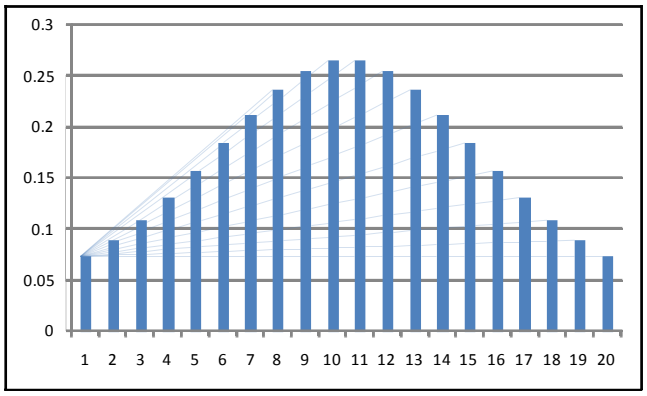

Figure 22: Distribution of quadrupole component (T/m) in the nonlinear magnet section.

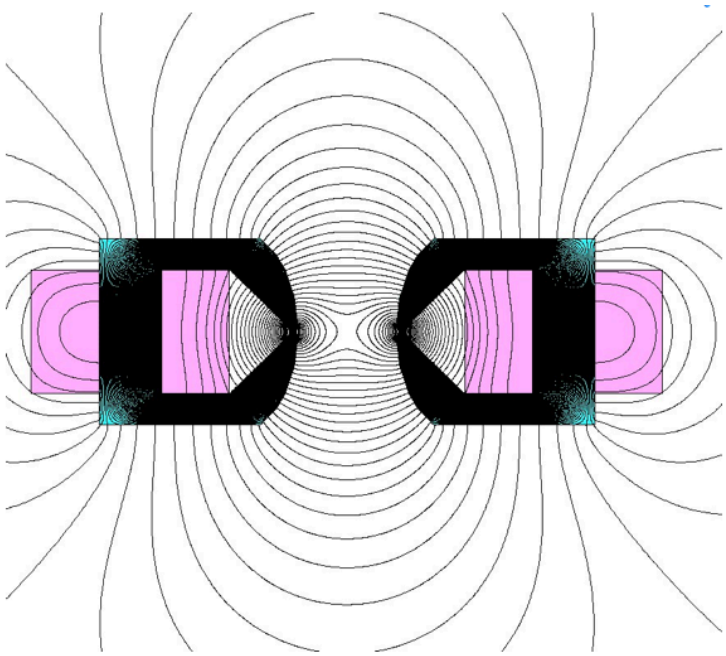

Figure 23: Cross-section of nonlinear magnet.

3.6.4.3 Vacuum System

Although studies of integrable optics require beam circulation only for 100,000 turns, other applications of the ring will demand beam lifetime of the order of 1 hour. This determines the specifications of the vacuum system, which must provide partial pressure of CO and H2 of 10^{-7} torr and 10^{-8} for Ar. The Aluminum beam pipe will have round cross-

section with 50 mm diameter in quadrupoles and dipole magnets, and elliptical shape 15×75 mm in the nonlinear magnet straight sections. Eight vacuum pumps will be attached to ports on the inside of dipole magnets.

3.6.4.4 Beam Diagnostics

Accurate tuning of the linear machine lattice is critical for proper functioning of the nonlinear integrable optics. The β-functions in the straight sections must be controlled to better than 5%, and tolerance on the betatron phase advance in the T-insert is 0.02. These requirements necessitate an extensive beam position monitoring system with 16 button-type pickups, capable of capturing the turn-by-turn beam position for 8-16 thousand turns with the precision of 100 μm.

Additionally, the ports in vacuum chamber in dipole magnets will provide points for synchrotron light based diagnostics.

3.6.4.5 RF System

We plan to adopt the Project X 162 MHz copper cavity design with some modifications. The RF cavity parameters are listed in Table 3.

Table 3: RF Cavity Parameters

Parameter	Value	Unit
Aperture diameter	50	mm
Frequency	162.45	MHz
Q factor	30877	
Shunt impedance	4.5×10^6	Ohm
Maximum voltage	50	kV
Power	0.56	kW

3.6.5 Status and Schedule

As of the time of this document (March 2012), the machine design requirements are finalized. The layout was selected, and most numerical simulations of particle dynamics in the final lattice have been performed. Components of beam instrumentation and vacuum system have been procured.The technical specification on elements of magnetic system and vacuum chamber were ready by February, 2012.

An external review of IOTA has been organized by Fermilab's Accelerator Physics Center (APC) and took place at Fermilab on 02/23/2012. The review committee was chaired by Prof A. Seryi of John Adams Institute (UK).

The committee reviewed all aspects of the IOTA experiment, including:

1) theoretical foundations of the IOTA method
2) numerical computer simulation of the beam stability in IOTA
3) overall design and plan of the experiment
4) technical preparedness of the design of key components of IOTA
5) schedule of implementation, cost and resources
6) plan of beam studies and experiments beyond Phase I

Particular focus was on items 3 and 4 (magnets, vacuum, RF, injection, diagnostics, power supplies, mechanical support and alignment, beam dump, safety, controls and overall integration).

All presentations, summary report and committee recommendation are available at https://indico.fnal.gov/conferenceDisplay.py?confId=5151

The committee recommended to proceed with procurement of the longest lead items (magnets for IOTA ring) in FY12 in anticipation that the ring assembly will take place during 2013, and beam commissioning will start in 2014. The committee report is given below in Appendix.

We would like to thank V. Kashikhin, G. Romanov (FNAL) and I. Batalov (MIPT) for their contributions.

3.7 Attosecond vacuum-ultraviolet pulses via space-charge-driven amplification of shot-noise density fluctuations

Over the past years, micro-bunching instabilities developing in high-brightness linear accelerator has received much attention as it hampers the performances of short-wavelength free-electron lasers. Such an instability develops due to the bunch self-interaction via longitudinal space charge and coherent synchrotron radiation. The micro-bunching effect has also been observed in standard beam diagnostics based on optical transition radiation.
Recently, it was proposed to control this instability to produce broadband radiation in the vacuum ultraviolet with attosecond durations.

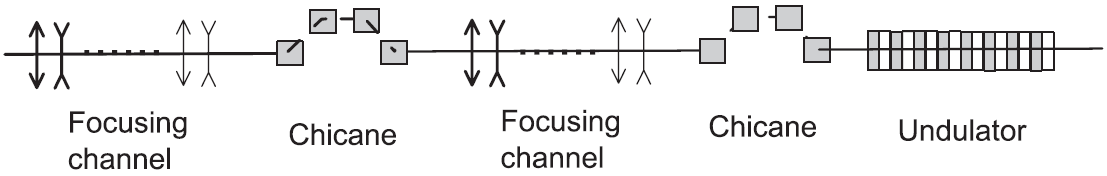

In the proposed scheme a series of longitudinal space charge amplifier (LSCA) modules are used; see Figure above. A LSCA module consists of a transversely focusing channel that act as a longitudinal drift followed by a magnetic chicane. In the longitudinal drift, energy modulations produced by the longitudinal space charge field accumulates. In the chicane these energy modulations are converted into density (current) modulations. One can associate a gain per LSCA module defined as the ratio of input over output density modulations. Several LCSA modules are consecutively used until the final modulation is on the order of unity. In the latter case the bunch current is fragmented and can radiates coherently at wavelength comparable to the characteristic size of the beamlets.

Reference [Dohlus, et al , 2011] provides a prescription for designing a system operating in the LSCA regime. Under optimum design, the typical gain of one LSCA module is

$$G \approx \frac{1}{\gamma\sigma_\delta}\sqrt{\frac{\gamma I_A}{I}},$$

where γ, σ_δ, I, and I_A are respectively the beam's Lorentz factor, rms intrinsic (uncorrelated) fractional momentum spread and peak current, and the Alfen current (17 kA). For the anticipated beam parameters at ASTA, gain values in excess of 10 are expected.. The optimum gain assumes the LSCA module is optimized to amplify density modulations with wavelength $\lambda \approx 2\pi\sigma_\perp/\gamma$ where $\sigma_\perp$ is the average rms transverse beam size in the longitudinal drift space.

Considering the case of ASTA in its operating phase II [E~500 MeV ($\gamma \approx 1000$)] and focusing the beam to 50 μm could result in density modulations with a wavelength on the order of 300 nm (this is the near-ultraviolet region of the spectrum but varying the beam size could also provide amplification from the vacuum ultraviolet to the optical regime -- the latter might be beneficial for experimental purpose especially while trying to understand the gain mechanism of an LCSA module). In order to enable the production of small transverse beam sizes we consider a FODO cell with average betatron function $\overline{\beta} = 2L/\sin\mu$=2 m where the half-length of the FODO cell and the betatron phase advance are respectively L=1 m and $\mu = \pi/2$. The total drift length of the LSCA should be $D \approx \gamma^2 \frac{\lambda}{2\pi}\sqrt{\frac{\gamma I_A}{I}}$~6 m which corresponds to 3 FODO cells. Finally, the optimum momentum compaction for the magnetic chicane is given by $R_{56} \approx \lambda/(2\pi\sigma_\delta)$. Achieving a net gain of 100 would conservatively require the cascading of three LSCA modules totaling a length of ~20 m (well within the real estate available during the phase II or III of ASTA).

A possible lattice for a cascaded LSCAwill need to be located downstream of ACC2. Upstream and downstream of the FODO channel, matching telescopes will respectively match the incoming beam's Courant-Snyder parameters into the FODO channel and match the outgoing parameters into the spectrometer beamline. The needed three magnetic chicanes could be inserted within half the length of a FODO cell (i.e. between two consecutive quadrupole magnets) as the typical required momentum compaction values are on the order of a few mm

maximum. Since these chicanes will not significantly perturb the lattice, one could practically envision a 20-m long FODO channel with chicanes inserted every 3-4 cells.

Finally, it is worth mentioning that as ASTA energy increases, the system could be scaled to micro-bunch at smaller wavelengths and eventually produces radiation in the vacuum ultraviolet regime (e.g. once ACC3 is installed). In addition, the present phase I configuration already include a FODO channel with average betatron function of 40 m this should amplify wavelengths in the THz regime and could therefore provide a first set of data on the experimental feasibility of the suggested scheme.

Cited reference :"Generation of attosecond soft x-ray pulses in a longitudinal space charge amplifier" M. Dohlus, E. A. Schneidmiller, and M. V. Yurkov, *Phys. Rev. ST Accel. Beams* **14**, 090702 (2011).

3.8 Potential for Critical Laser-Induced Microbunching Studies with the High-Micropulse-Repetition-Rate Electron beams at ASTA – updated 7/24

[Alex H. Lumpkin and Jinhao Ruan, FNAL; John M. Byrd and Russell B. Wilcox, LBNL;
submitted December 12, 2011 – updated July 24, 2012]

3.8.1 Abstract

Investigations of the laser-induced microbunching as it is related to time-sliced electron-beam diagnostics and high-gain-harmonic generation (HGHG) free-electron lasers using bright electron beams are proposed for the ASTA facility. Initial tests at 40-50 MeV with an amplified 800-nm seed laser beam co-propagating with the electron beam through a short undulator (or modulator) tuned for the resonance condition followed by transport through a subsequent chicane will result in energy modulation and z-density modulation (microbunching), respectively. The latter microbunching will result in generation of coherent optical or UV transition radiation (COTR, CUVTR) at a metal converter screen which can reveal slice beam size, centroid, and energy spread. Additionally, direct assessment of the microbunching factors related to HGHG by measurement of the COTR intensity and harmonic content after the chicane as a function of seed laser power and beam parameters will be done. These experiments will be performed using the ASTA 1-MHz-rate micropulse train for up to 1ms which is unique to test facilities in the USA.

3.8.2 Introduction

We have identified critical aspects of laser-induced microbunching (LIM) to be explored at the Advanced Superconducting Test Accelerator (ASTA) which relate directly to time-sliced electron-beam diagnostics and seeded free-electron laser (FEL) issues. In the first category the capability of evaluating the electron beam parameters such as beam size, centroid, and energy

spread as well as the microbunching factors in sub-ps time slices should be possible by imaging the LIM coherent optical and UV transition radiation (COTR, CUVTR). In the second category, enhanced performance in gain length, spectral bandwidth, central wavelength stability, etc. of free-electron lasers (FELs) can be obtained by seeding the FEL either with electron beam microbunching at the resonant wavelength as in the case of high gain harmonic generation (HGHG), cascaded HGHG, and echo-enhanced harmonic generation (EEHG) [1-3] or by generating a photon beam at short wavelengths such as from a plasma as in high harmonic generation (HHG)[4]. These seeding processes are initiated by co-propagating a laser beam with the electron beam through a short undulator (modulator) tuned to the seed wavelength to generate an energy modulation which is then converted to a z density modulation (microbunching) in a dispersive section such as a chicane. It has been found that the electron beam is also microbunched at the harmonics of the laser fundamental after the chicane, and the radiator undulator is tuned to one of them for the FEL [1]. Yu et al. have reported lasing on the 3rd harmonic of the laser fundamental of 800 nm, and FERMI@Elettra staff have reported recent HGHG results out to the 13th harmonic of 266 nm [5]. The direct measurement of the microbunching by looking at the coherent optical and UV transition radiation (COTR) was first done in a SASE FEL [6], but microbunching generated by LIM has rarely been measured [7]. Moreover, high harmonic content has not been directly observed, but it has been deduced from the HGHG radiator results [8]. Direct microbunching measurements have been proposed on the SDUV FEL in Shanghai [9], and discussions are underway with FERMI@elettra staff for VUV tests on their HGHG FEL. Elucidating the harmonic content, optimizing it, and benchmarking codes would be critical to present and future short wavelength (VUV-soft x-ray) FEL projects based on HGHG or EEHG. Only ASTA has the high-micropulse-repetition rate (1 MHz for 1 ms) beam such as proposed for the next generation of FELs [10], albeit with higher duty factor for the latter.

Our emphasis in this report is on the use of COTR (ultimately CVUVTR) as a direct microbunching diagnostic with the potential for time–resolved electron beam diagnostics and for benchmarking relevant FEL codes. As context, we point out that there are at least three mechanisms for generating optical-regime microbunching (which can be extended to the VUV) in an electron beam:

1. longitudinal-space-charge-induced microbunching (LSCIM): This mechanism has been suggested by Saldin et al. [11] to contribute more in the visible wavelength regime than coherent synchrotron radiation (CSR) or wakefields. This effect can be considered as starting from shot noise in the charge distribution that couples through the longitudinal impedance of the transport line and linac into an energy modulation. This energy modulation will become a z-density modulation, or microbunching, after bunch compression in a chicane (or other R_{56} lattice point) [12]. It is generally a broadband effect in wavelength, and most of the gain is in the FIR (>10-µm regime). However, we have the LCLS/SLAC [13], APS/ANL [14], FLASH/DESY [15], and FERMI@Elettra [16] results on COTR in the OTR images and even scintillator screens. Spatially localized enhancements of 10-10,000 at visible wavelengths have been reported which prevent using the standard beam profiling techniques with optical beam images.

2. laser-induced microbunching (LIM): a) where an external laser beam is injected into the beamline so it copropagates with the electron beam through a short undulator (the modulator) which interaction modulates the beam energy that then becomes a z-density modulation after

a dispersive element such as in a chicane and b) where the seeding of an FEL with an external laser or harmonic at the long radiator undulator itself. The former results in narrowband microbunching and is used to prebunch or seed the beam for the FEL, and the latter is used as input to an FEL amplifier. The main objective of these proposed studies is measuring LIM.

3. SASE-induced microbunching (SIM) which is the fundamental mechanism of the self-amplified spontaneous emission (SASE) FEL process starts from noise when the SASE photon fields acting with the undulator fields on the electrons result in the growth of electron beam microbunching and concomitant exponential growth of SASE light at the resonant wavelength and harmonics. This is a narrowband effect. We note evidence for the LSCIM from the linac providing prebunched beam on experiments in the APS visible SASE FEL [17]. This demonstration actually links to the HGHG process via the principle of a prebunched beam's enabling FEL startup, as opposed to startup from noise as in a SASE FEL. Historically, LSCIM and SIM COTR were modeled after the first experiments, but in the LIM case we have more modeling in place before extensive experiments have been performed. We also expect to take advantage of techniques developed for the earlier modes.

3.8.3 Laser-Induced Microbunching

The initial step in HGHG is co-propagation of a seed laser with the electron beam through a short undulator or modulator tuned to resonance as indicated schematically in Fig. 1. The laser pulse length can be used to modulate a time slice of the transverse distribution or it could be lengthened to provide modulation over the whole e-beam pulse length. At 40 MeV it is impractical to satisfy the resonance condition for an 800-nm wavelength on the fundamental of an undulator based on permanent magnets. For a planar undulator, the FEL process is governed by the resonance condition:

$$\lambda = \lambda_u (1 + K^2/2)/2n\gamma^2, \qquad \text{Eq. 1}$$

where λ is the FEL wavelength, λ_u is the undulator period, K is the undulator field strength parameter, n is the harmonic number, and γ is the relativistic Lorentz factor.

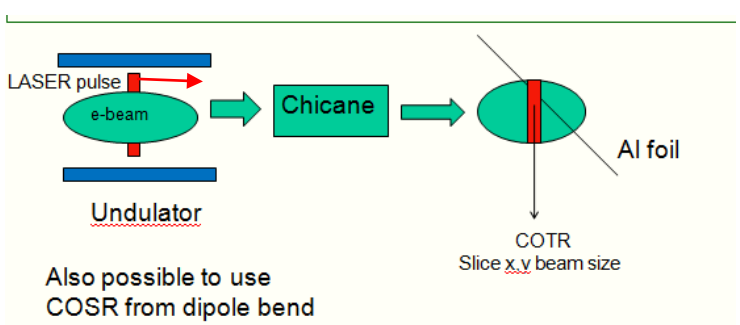

Figure 1: Schematic of laser-induced energy modulation followed by the dispersion in the chicane to produce a microbunched beam that can generate COTR or COSR in a slice. In principle the entire e-beam profile could be microbunched as well for HGHG.

However, it has been calculated that there is reasonable coupling strength at the third harmonic of the planar undulators as shown in Fig. 2 from reference [18]. The coupling coefficients JJ_n for n=1,3,5 versus K are reasonable, although with a rapid decrease in their

values below *K*=1.5 for n=3,5 for the 780-nm case. We suggest with this concept we could modulate the energy at 800 nm in an undulator with period 1.8 cm using the third harmonic coupling of ~0.25 and then generate harmonics of the laser wavelength in the microbunching in the dispersive section. Initially, we would use visible-UV optics to detect n=2,3,4 at 400, 266, and 200 nm, respectively, in the Phase 1a experiments. Subsequently we would look for the critical higher harmonics in the VUV with appropriate diagnostics in Phase 1b as will be discussed in a later section. (Due to available 1054-nm lasers now at FNAL and LBNL, there may be some practical advantages for shifting to this wavelength. However the present S20 PC streak camera tube is insensitive at 1054 nm, it is difficult to chirp the IR beam to generate few-ps pulses to cover the electron beam longitudinally, and the harmonic wavelengths will be 20% longer than the reference case. Further evaluation of this aspect is needed.)

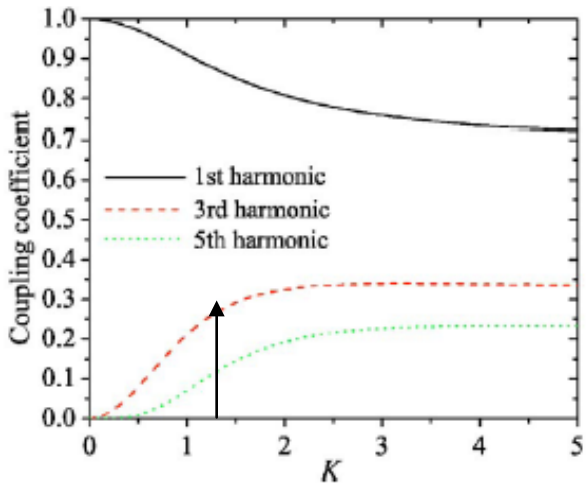

Figure 2: Coupling coefficients for odd harmonics for a planar wiggler as a function of *K*. The γ=80 case with *K*=1.20 is indicated by the arrow. [18]

3.8.4 Coherent Optical Transition Radiation

A brief review of the source of the COTR, CUVTR, CVUVTR, etc. is in order. Transition radiation is emitted when a charged particle beam crosses the interface between two media with different dielectric constants, such as vacuum to a metal. It is a surface phenomenon, and the production time is estimated in the few-fs regime. Normally, incoherent OTR is a broadband phenomenon, but the special conditions of LIM lead to narrow band COTR. We propose that the simple modeling developed for SIM COTR [19] can be applied to LIM COTR. The coherent spectral angular distribution is given by the product of the reflection coefficients, the single electron spectral angular distribution, the interference term if applicable, and the coherence function which will be described below:

$$\frac{d^2N}{d\omega d\Omega} = \left|r_{\perp,//}\right|^2 \frac{d^2N_1}{d\omega d\Omega} I(\mathbf{k})\Im(\mathbf{k}) \qquad \text{Eq. 2}$$

where the single electron spectral angular distribution is given by,

$$\frac{d^2N_1}{d\omega d\Omega} = \frac{e^2}{\hbar c}\frac{1}{\pi^2\omega}\frac{\left(\theta_x^2+\theta_y^2\right)}{\left(\gamma^{-2}+\theta_x^2+\theta_y^2\right)^2} \qquad \text{Eq. 3}$$

The coherence function is given by:

$$\Im(\mathbf{k}) = N + N_B\left(N_B - 1\right)\left|H(\mathbf{k})\right|^2 \qquad \text{Eq. 4}$$

with the Fourier transform of the charge form factors being,

$$H(\mathbf{k}) = \frac{\rho(\mathbf{k})}{Q} = g_x(k_x)g_y(k_y)F_z(k_z) \qquad \text{Eq. 5}$$

and where Q is the total charge and $f_B = N_B/N$ is the bunching fraction. Note the coherence function reduces to just the number of particles, *N*, when the number of microbunched particles N_B *is zero* in this formalism. We expect significant fractions from the LIM process, and hence order of magnitude enhancements of COTR.
The transverse form factors are for *i=x,y,*

$$g_i(k_i) = \frac{1}{\sqrt{2\pi}}e^{-\sigma_i^2 k_i^2/2} \qquad \text{Eq.6}$$

and the longitudinal form factor for a train of *M*+1 micropulses

$$\tilde{F}(k_z') = f(k_z')\sum_{m=0}^{M} e^{-ik_z' m\ell} = f(k_z')\frac{\sin\left(Mk_z'\ell/2\right)}{\sin\left(k_z'\ell/2\right)} \qquad \text{Eq.7}$$

with the longitudinal form factor for an individual microbunch

$$f(k_z) = \frac{1}{\sqrt{2\pi}}e^{-\sigma_z^2 k_z^2/2} \qquad \text{Eq. 8}$$

Ratner, Chao, and Huang [18] have considered LSCIM COTR in their modeling, and related the effects to the bunching fractions in Eq. 9. The first term in the square bracket is the incoherent OTR, and the second term is the coherent contribution due to microbunching with bunching factor $b_c(\boldsymbol{k})$. In their model the OTR spectral gain is the ratio of the angle-integrated second term over the angle integrated first term. The solid angle of their optics is given by ϑ_m. One can obtain significant gain for bunching fractions of only a few per cent, needless to say, when *N* is large as in a 250 pC micropulse.

$$\frac{dW}{d\omega} = \int_{-\theta_m/2}^{\theta_m/2} d\theta_x \int_{-\theta_m/2}^{\theta_m/2} d\theta_y \times \left(\frac{d^2W}{d\omega d\Omega}\right)_1 \left[N + N^2|b_c(\boldsymbol{k})|^2\right] . \qquad \text{Eq. 9}$$

They considered the longitudinal space charge impedance of their S-band linac, the chicane's R_{56}, the energy chirp, slice energy spread, and other factors. For the broadband instability and a 3-keV slice energy spread they would see gains/enhancements in the red curve over incoherent OTR (blue curve) as represented in Fig. 3 [14].

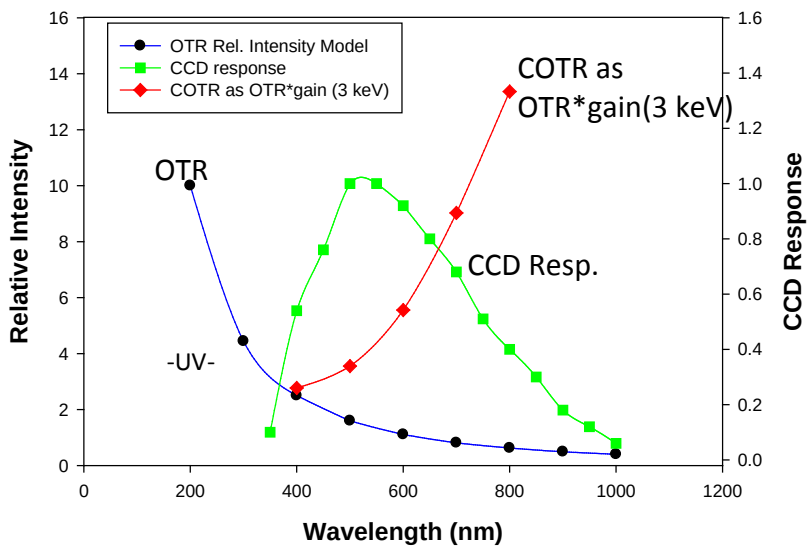

Figure 3: Plots of the nominal OTR intensity dependence on $1/\lambda^2$, the COTR intensity using the calculated gain factor at LCLS for a 3-keV slice energy spread [14,20], and the nominal CCD camera relative response.

These considerations describe the gain expected with LSCIM, but the narrowband nature of LIM may be best illustrated by showing the results of the narrowband microbunching in the SIM experiments at APS/ANL in 2002. Figure 4 shows a composite of the spectra obtained for a visible FEL operating near 535 nm [6]. The COTR spectra on the left are narrowband, but not quite as narrow as the SASE also observed after undulator 5 of nine undulators. The bunching fraction at saturation was calculated at about 20% of the e-beam, and enhancements of 10^4 for COTR and 10^6 for SASE were obtained. As we understand it bunching fractions of 5-10 % could be obtained in HGHG and EEHG configurations, even for harmonics of n=10 or 50, respectively. The potential for measuring the resultant enhanced transition radiation and elucidating LIM is high. We note that the bunching fractions would also apply to enhancing coherent optical synchrotron radiation (COSR), coherent undulator radiation (CUR), and coherent optical diffraction radiation (CODR) which mechanisms provide the potential for nonintercepting beam diagnostics for the high power beam mode of ASTA.

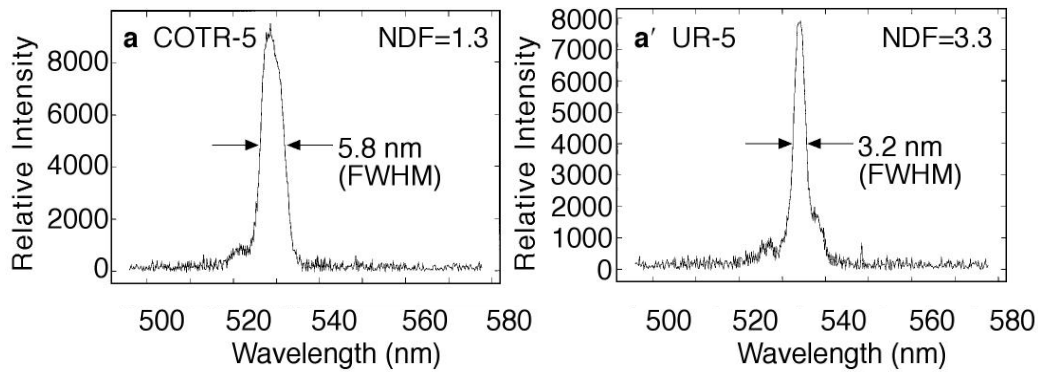

Figure 4: Example COTR (L) and SASE (R) spectra from the visible FEL experiments at ANL sampled after undulator 5 with SASE saturation occurring at about undulator 5. The SASE is 100 times brighter than COTR, but involved 365 undulator periods versus 2 transition radiation converter interfaces [6].

3.8.5 Proposed studies

The ASTA linac with photocathode (PC) rf gun, two booster L-band SCRF accelerators (CC1 and CC2), and beamline is schematically shown in Fig. 5. The L-band accelerating sections will provide 40- to 50-MeV beams before the chicane, and an additional acceleration capability up to a total of 800 MeV will eventually be installed in the form of three cryomodules with eight 9-cell cavities with average gradient of 31 MV/m after the chicane. The phase of the CC2 section can be adjusted to energy chirp the beam entering the chicane to vary bunch-length compression. Maximizing the FIR coherent transition radiation (CTR) in a detector after the chicane will be used as the signature of generating the shortest bunch lengths. Micropulse charges of 20 to 3200 pC will be used typically. The nominal pulse format for high power ILC-like beam is 3.2 nC per micropulse at 3 MHz for 1 ms. The macropulse repetition rate will be 5 Hz. For the 1-ms period the pulse train micropulse spacing can be at a higher rate than a proposal of 100 kHz in any one of ten FEL beamlines. This aspect

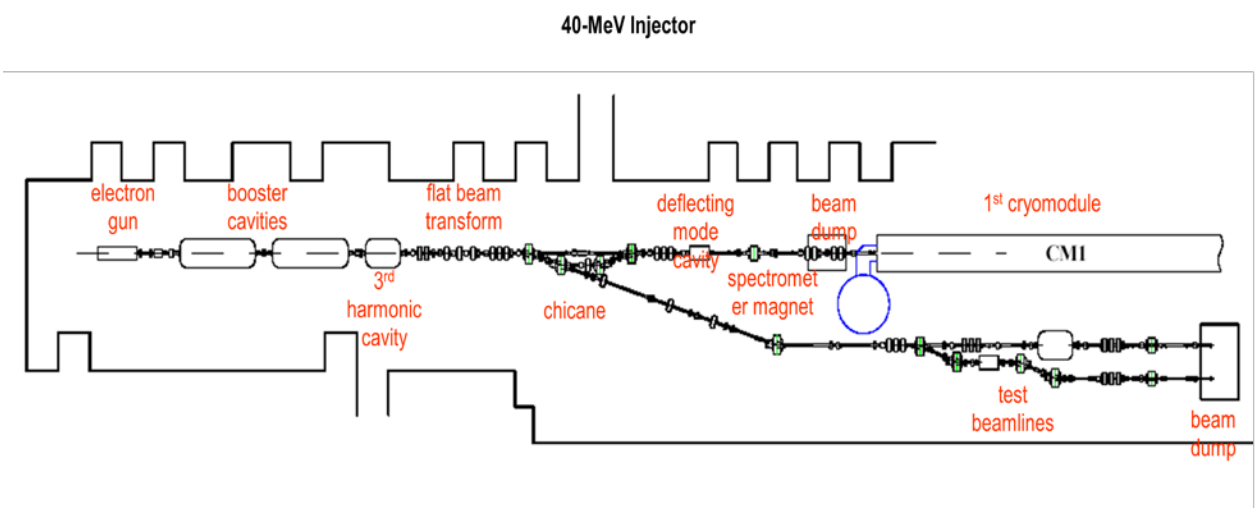

is unique for test facilities in the USA and highly relevant to the next generation of FELs.

Figure 5: Schematic of the injector for the ASTA facility showing PC rf gun, booster accelerators, and beamlines. The first LIM tests are proposed in the test beamline as schematically indicated by the 800-nm laser beam injection into the beamline, modulator, chicane, and COTR diagnostics station locations. The Visible-UV streak camera could be used for both laser synchronization and COTR measurements.

3.8.6 Phase 1

We would start Phase 1 at 40-50 MeV with an 800-nm seed and a modulator with about 1.8 to 2.2 cm period, K~1.2, and with length about 1 m. (The loan from LBNL of two or three 0.5-m sections with 2.18 cm period is under discussion.) The experiment location is shown in Fig. 5. We would need to use resonance at the 3rd harmonic of the planar undulator as explained earlier. This is a key, and confirmation of this approach and modeling of the expected microbunching is recommended. We would need an amplifier for the 100 kHz 800-nm laser beam from the ASTA Ti:Sa laser or doubled- frequency Erbium Fiber laser to provide about 200-500 µJ per pulse, although we could start with fewer pulses in the pulse train initially. An optical parametric amplifier (OPA) could do this in principle. A laser concept developed for the EOS experiments envisioned for ASTA is shown in Fig. 6. The pump laser is an existing Nd:YLF operating at 1 MHz. One might obtain higher energy pulses at the lower repetition frequency of 100 kHz and for longer pulses. The pulse train also might be shortened for initial tests. LBNL would collaborate on a solution for the OPA. The modulator should fit after the dogleg entering the low-energy test beamline at ASTA with diagnostics at both ends to align the laser and electron beam transversely. The FNAL Visible-UV streak camera would be used for timing the laser with the UR or OTR within the modulator to 1 ps or better. We have successfully done this in recent EOS tests at A0PI with the 800 nm Ti:Sa and incoherent OTR signals [21]. It also might be used to look directly at the LIM COTR within the micropulse as generated at the test station. (The system temporal resolution will be improved with narrow bandwidth COTR and also might be extended with a deflecting mode cavity [7].) The chicane configuration that is planned for an emittance exchange (EEX) could presumably be used with its tunable R_{56} [22], but this needs to be checked. Visible-UV diagnostics would be needed after the Chicane to measure the harmonics n=2,3,4 of 800 nm at 400, 266, and 200 nm, respectively.

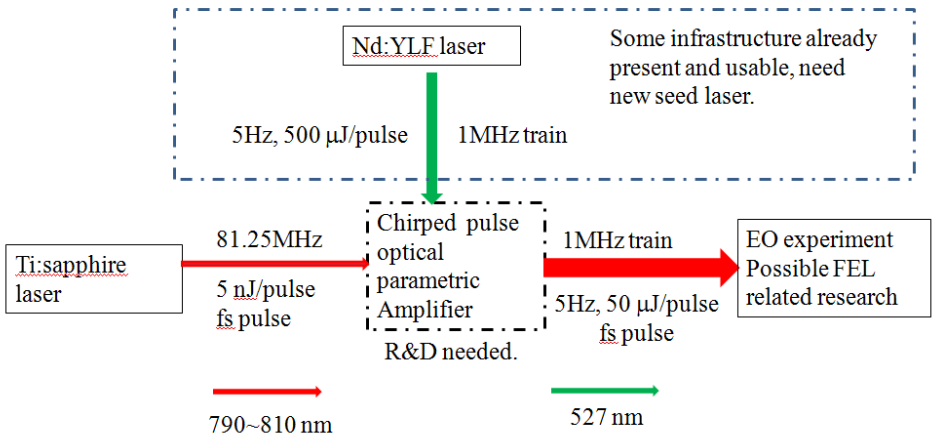

Figure 6: Schematic of the proposed ASTA diagnostics laser with OPA indicated. The pulse length and wavelengths need to be evaluated for microbunching tests. This laser system is being considered for the downstream diagnostics lab to support electro-optic tests.

In Phase 1b we would use VUV diagnostics since codes generally indicate harmonics of n~10 should be generated. An available in-vacuum flange-mounted 40-mm diam microchannel plate (MCP) has been identified as a candidate 2D imager that has sensitivity from 1 eV to 50 keV. The output P43 phosphor would be viewed by a standard CCD camera, and two-dimensional images of the VUV angular distribution could be recorded. These should indicate laser/e-beam angular overlap which has been shown to impact SIM microbunching and FEL gain [23]. Evaluation of the LBNL multilayer metal mirrors at various VUV wavelengths, and testing of their robustness to electron-beam pulse trains would be of interest. As an alternative the multilayer mirrors might be located after the downstream dipole to eliminate e-beam bombardment. Development of VUV filtering schemes would also be tested. Additionally, one could use laser pulses shorter than the e-beam micropulse to probe the slice transverse beam size and centroids of the electron beam or map out the longitudinal profile as previously demonstrated at FLASH [24]. More detailed harmonic information should be obtained by use of imaging spectrometers in the UV and VUV (McPherson version has a series of gratings to use and an imaging array for display). This would provide the ultimate diagnostic of the microbunching harmonics' central wavelengths and spectral widths. LBNL would have or provide the OPA for the FNAL Ti:sapph laser oscillator, the modulator system in principle (informal discussion), the VUV mirrors, and possibly the VUV spectrometer. They also have the needed modeling capability for the HGHG and EEHG FEL processes which should include calculation of microbunching factors entering the radiator.

3.8.7 Phase 2

In Phase 2 we would move to the high-energy test lines, and the seed laser could be located in the downstream laser room. We may consider shifting to amplified 266 nm seed and look for n=10, but we should be able to start at 800 nm on the fundamental with a 20-cm-period undulator for an e-beam energy of 250 MeV. Depending on beam energy and undulator period we should be able to reach the VUV to soft x-ray regime in the microbunching. Only ASTA in the

USA has the pulse train to test the technique at 100 kHz as needed, as well as the low energy jitter of a SC linac to enable generation and averaging of higher harmonics. We estimate HGHG and EEHG might be explored in a high-energy test line within a 12-15 m zone, but cascaded HGHG could be tight. At one time 30 m of z space was indicated as usable, and various configurations should be explored. A schematic is shown in Fig. 7 of the layout of the simplest. With 900 MeV (4 cryomodules plus injector) and a short period undulator (maybe SCU) we could ultimately reach a few nm in the beam and the radiator. This should have strong relevance for future FELs in general.

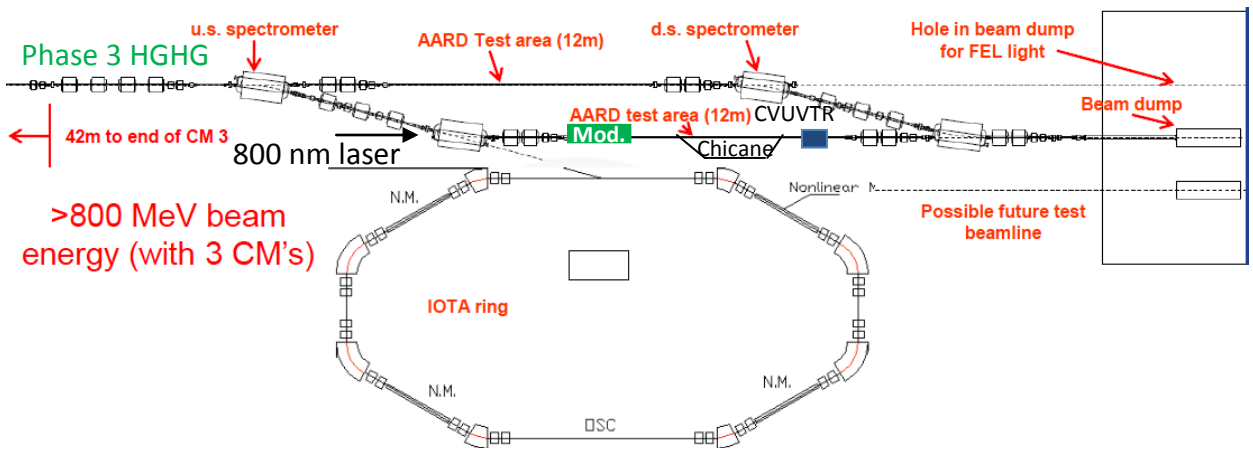

Figure 7: Schematic of the simplest microbunching experiment layout in the high-energy area. The possible configurations for HGHG and EEHG should also be considered.

Table I summarizes some of the configurations for the proposed studies. In some cases we are only concerned about looking at the microbunching in the electron beam post chicane so the radiator needed for HGHG is not a constraint. Phase 1 could be started in FY14 if agreements can be made soon so preparations can be made in FY13. The EEHG case is not determined yet, but we are looking for an n=100 demonstration where the radiator has a short period. The last SASE case at 900 MeV invokes the use of a 4-m-long SC undulator [25] with period 1.1 cm and *K*=0.92 to generate radiation and microbunching at 3 nm as a test since we would not have 2.5 GeV available. Separating the CXTR and SASE sources is a technology challenge to be addressed for this case.

Table I: Summary of possible microbunching experiments at ASTA at 40-45 MeV and higher energies following the cryomodules. The potential observation wavelengths of several of the harmonics are indicated.

Phase #	Beam Energy (MeV)	Laser Fundamental (nm)	Und. Period (cm), K, n	Microbunching Harmonics (nm)
1a	44.5	800	2.18, 1.2, 3	400,266, 200
1b	44.5	800	2.18, 1.2, 3	100,90,80
2	250	800	20.0,1.36,1	400,266,200,80

2	200	266	5,1.2,1	48,29,26
2-SASE	500	----	5,1.2,1	42,14
3-HGHG	900	TBD	TBD	--
4-SASE	900	--	1.1,0.9,1	3
EEHG	900	--	TBD	

3.8.8 Summary

In summary, we have described how a series of direct LIM experiments with diagnostics in the optical, VUV, and soft x-ray regime could be implemented at the ASTA facility. This is the only facility in the USA that has the pulse train of at least 100 kHz repetition rate to simulate proposed FEL configurations. These experiments should extend understanding of the critical phenomena of microbunching harmonic generation and preservation and allow benchmarking of codes. The potential use for HGHG and EEHG FELs at several nm with scalable results is targeted. In addition, the as-described sub-micropulse electron-beam diagnostics based on COTR could be developed into nonintercepting electron beam diagnostics if used with the COSR, CUR, or CODR mechanisms.

Notes: Assumed 50-MeV User beamline for EEX installed with chicane with tunable R_{56}: FNAL streak camera and UV diagnostics; one meter long undulator with stand (loan from LBNL); FNAL in-vacuum MCP for VUV detection; seed laser transport line to modulator ($25k); Miscellaneous optics (15K).

Long range: propose VUV McPherson spectrometer ($75k) with readout camera. Need cryomodules installed and beam transport to high energy end test locations. Re-locate 1-m long undulator or other.

3.8.9 References

1. L.H. Yu et al., Phys. Rev. Lett. 91, 074801, (2003).
2. Z. Zhao et al., "Seeding Experiments at the SDUV-FEL", WEOB2, Presented at FEL11, August 24, 2011.
3. G. Stupakov, PRL 102, 074801, (2009).
4. G. Lambert et al., "High Harmonics from Gas", MOOBI2, Presented at FEL11, Aug.24-27, 2011.
5. E. Allaria et al., "FEL Commissioning at FERMI@Elettra, Presented at FEL 11,WEOBI1, Shanghai, China, Aug.24-27, 2011.
6. A.H. Lumpkin et al., PRL 88, 234801, (2002).
7. D. Xiang et al., Phys. Rev. ST –AB, 14, 112801 (2011).
8. Z. Zhao et al., "Seeding Experiments at the SDUV-FEL", WEOB2, Presented at FEL11, August 24, 2011.
9. A.H. Lumpkin, seminar presented at SINAP, Shanghai, China, Aug. 17, 2011.
10. See contributions to "Realizing the Potential of Seeded FELs in the Soft X-ray Regime Workshop", Berkeley, CA, Oct. 26-28, 2011.
11. E.L. Saldin, E.A. Schneidmiller, and M.V. Yurkov, DESY Report No. TESLA-FEL-2003-02, 2003.
12. Z. Huang et al., PRST-AB 7, 074401 (2004).
13. D.H. Dowell et al., "LCLS Injector Commissioning Results", Proc. of FEL07, Aug. 26-30, 2007, Novosibirsk; R. Akre et al., Phys.Rev.ST-AB 11, 030703 (2008).

14. A.H. Lumpkin, N.S. Sereno, W. Berg, M. Borland, Y. Li, and S. Pasky, "Characterization and Mitigation of Coherent Optical Transition Radiation Signals from a Compressed Electron Beam, Phys. Rev. ST-AB 12, 080702,(2009).
15. M. Yan et al., "Beam profile Measurements Using a Fast Gated CCD Camera and Scintillation Screen to Suppress COTR", THPB16, presented at FEL 11, Shanghai China, Aug.24-27, 2011.
16. M. Veronese and E. Allaria, WEPB23, presented at FEL11, Shanghai, China, Aug.24-27, 2011.
17. A.H. Lumpkin, R.J. Dejus, and N.S. Sereno, Phys. Rev. ST-AB, 12, 040704 (2009).
18. P. Musumeci, C. Pellegrini, and J.B. Rosenzweig, Phys. Rev. E 72, 016501 (2005).
19. D. W. Rule and A.H. Lumpkin, "Analysis of COTRI Patterns Produced by SASE-Induced Microbunches", Proc. of PAC2001,1288 (2001).
20. D. Ratner, A. Chao, and Z. Huang, "Three-Dimensional Analysis of Longitudinal Space Charge Microbunching Starting from Shot Noise", Proc. of FEL08, Gyeongju, Korea, Aug. 24-29, 2008.
21. T. Maxwell et al., "Single-shot Electro-optic Sampling of CTR at the A0 Photoinjector", Proc. of IPAC11, Sept. 2011.
22. P. Piot, FNAL AAC Review, Nov. 6, 2011.
23. Y.-C. Chae, A.H. Lumpkin, M. Erdmann, J.W. Lewellen, and S.V. Milton, "An Experimental Study of the Beam-steering effect on the FEL Gain at LEUTL's Segmented Undulators", Proc. of FEL 2004, Trieste Italy, 100, (2004).
24. G. Angelova et al., PRST-AB,11, 070702 (2008).
25. E. Baynham et al., Proc. of PAC09, WE2RAI01, (2009).

3.9 Feasibility of an XUV FEL Oscillator at ASTA – new 7/26

[Alex H. Lumpkin, FNAL, submitted July 26, 2012]

3.9.1 Abstract

The projected pulse format with a micropulse repetition rate of 3 MHz for an ultrabright electron beam of GeV-scale energies at the Advanced Superconducting Test Accelerator (ASTA) facility could enable the *first* XUV free electron laser (FEL) oscillator experiments. Concepts based on combining such beams with a suitable undulator and optical resonator cavity for an FEL are described. In addition preliminary single-pass studies using undulator radiation (UR) as a nonintercepting diagnostics technique for bright electron beams are presented. Initial studies at visible wavelengths would be done for 125-MeV electron beams using an undulator with period of 4-5 cm, magnetic structure length of 4.5 m, and tunable field parameter, *K*. Standard time-resolved imaging techniques would be employed to evaluate beam size, position, emittance, bunch length, phase, and energy during the macropulse. Extension of the techniques to higher energy beams using the corresponding UV and VUV UR will also be described.

3.9.2 Introduction

One of the challenges of the present-day and proposed superconducting linear accelerators with concomitant high-power beams is identification of unique applications for those beams. The high-power electron beams for the Advanced Superconducting Test Accelerator (ASTA)

facility involve up to 3000 micropulses at a 3 MHz repetition rate with up to 3.2 nC per micropulse in a 1-ms macropulse in the ILC-like mode [1]. With beam energies projected from 45 to 800 MeV, various beam dynamics issues will be addressed, but it is proposed such a beam in a lower-charge and low-emittance mode could also uniquely drive the *first* extreme ultraviolet (XUV or EUV) free-electron laser (FEL) oscillator experiments. These anticipated transform-limited photon pulses in wavelength and pulse length would address issues of limited bandwidth inherent to the self-amplified spontaneous emission (SASE) FELs that start from noise and should be competitive with seeded FELs as discussed in a recent LBNL-SLAC workshop [2]. An existing undulator case is combined with a previously suggested ring resonator optical configuration [3,4] or a concentric cavity optical configuration that in principle could fit the FEL in the ASTA tunnel. Preliminary estimates are reported for the FEL oscillator power saturation at 42 nm and 13.4 nm with scaling to shorter wavelengths with higher beam energies and shorter period undulators.

In preparation for the multi-pass FEL tests, single-pass experiments are also proposed that provide the non-intercepting diagnostics of the beam size, emittance, energy, bunch length, and phase. The acquisition of a comprehensive set of electron beam properties from a linear accelerator based on undulator radiation (UR) emitted from a 5-m long device was demonstrated over two decades ago on a visible wavelength free-electron laser (FEL) [5] driven by a pulse train of 100-µs extent. Comparable investigations were performed using x rays with a dedicated diagnostics undulator on two storage ring projects [6,7]. The high-power electron beams of the ASTA facility with beam energies projected from 45 to 800 MeV will need non-intercepting diagnostics. Besides the rf BPMs, optical synchrotron radiation (OSR), and optical diffraction radiation (ODR) techniques already considered, I propose the use of the properties of undulator radiation from a dedicated device for diagnostics with a nominal period of 4-5 cm, a tunable field parameter *K*, and a length of several meters. One proposes time resolving the e-beam properties within the macropulse by viewing the undulator radiation with standard electronic-shuttered CCDs or gated ICCD's (size and position) and a synchroscan streak camera coupled to an optical spectrometer (energy, bunch length, and phase). The feasibility of extending such techniques in the visible regime at a beam energy of 100-125 MeV into the UV and VUV regimes with beam energies of 250 and 500 MeV will be presented.

After discussion of the single-pass mode aspects, I introduce considerations of taking full advantage of the ASTA electron beam's 3-MHz micropulse repetition rate and 6-dimensional ultrabright beam quality to drive the first XUV FEL oscillator using a ring resonator optical configuration. This would be a unique opportunity to shatter the existing short-wavelength record of 176 nm in an FEL oscillator [8], and such a demonstration would impact the designs of the next generation of light sources.

3.9.3 Conceptual Aspects of Undulator Radiation

The propagation of the electron beam through the alternating magnetic fields of an undulator results in electron beam trajectory oscillations and the generation of co-propagating photons as schematically shown in Fig. 1. This is initially through the spontaneous emission radiation (SER) process, but under the right conditions in a long undulator a favorable instability evolves, and the electron beam is microbunched at the resonant wavelength leading to a self-amplified spontaneous emission (SASE) FEL. This intrinsic SASE-induced microbunching (SIM) is

fundamental to all SASE FELs and analogous microbunching occurs in all FELs. For a planar undulator, the radiation generation process on axis is governed by the resonance condition:

$$\lambda = \lambda_u (1 + K^2/2)/2n\gamma^2, \qquad \text{Eq. 1}$$

where λ is the UR wavelength, λ_u is the undulator period, $K = e\, B_0 \lambda_u / 2\pi\, mc = 0.934\, \lambda_u$ (cm) B_0 (T) is the undulator field strength parameter (B_0 is the magnetic field in the gap, *e* and *m* are the electron charge and mass, and *c* is the speed of light), n is the harmonic number, and γ is the relativistic Lorentz factor.

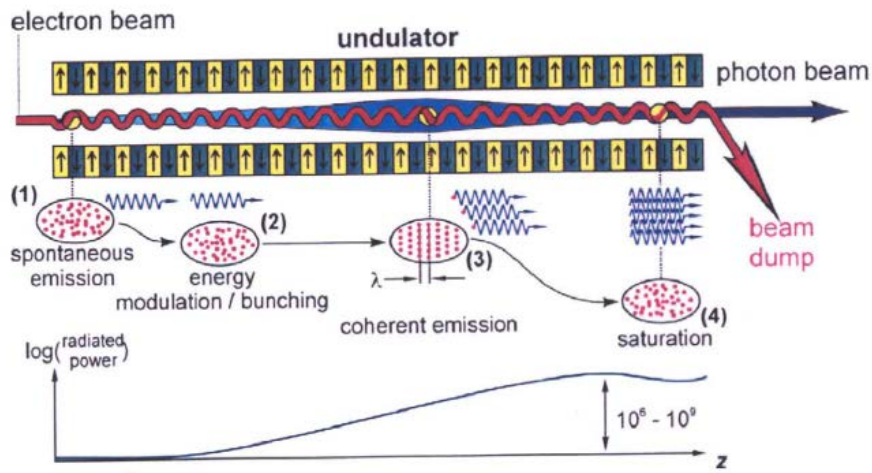

Figure 1: Schematic of the generation of undulator radiation for SER and SASE mechanisms [9].

Additionally, it has been calculated that there is coupling strength for energy exchange between the copropagating electrons and the photon fields at the third harmonic of the planar undulators as shown in Fig. 2 from reference [10]. The coupling coefficients JJ_n for n=1,3,5 versus *K* are reasonable, although with a rapid decrease in their values below *K*=1.5 for n=3,5. This indicates that the generation and measurement of these harmonics may in some cases be advantageous, particularly if the goal is to reach shorter wavelengths for a given beam energy.

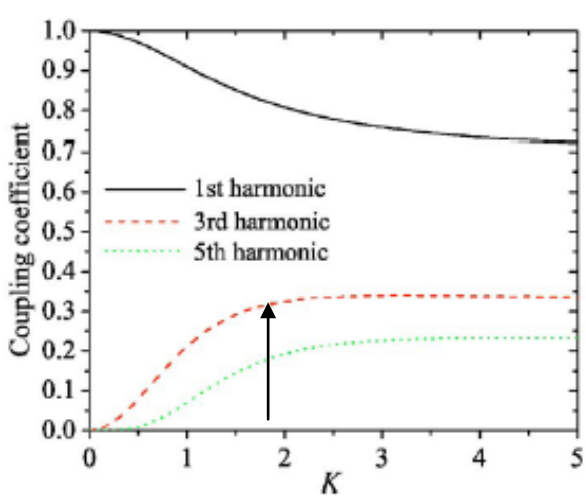

Figure 2: Coupling coefficients for odd harmonics for a planar wiggler as a function of *K*. The γ=500 case with *K*=1.8 is indicated by the arrow. [10]

3.9.4 Proposed Studies

The ASTA linac with photocathode (PC) rf gun, two booster L-band SCRF accelerators (CC1 and CC2), and beamline will provide 40- to 50-MeV beams before the chicane, and an additional acceleration capability up to a total of 800 MeV will eventually be installed in the form of three cryomodules with eight 9-cell cavities with average gradient of 31 MV/m after the chicane. The phase of the CC2 section can be adjusted to energy chirp the beam entering the chicane to vary bunch-length compression. Maximizing the FIR coherent transition radiation (CTR) in a detector after the chicane will be used as the signature of generating the shortest bunch lengths. Micropulse charges of 20 to 3200 pC will be used typically. The nominal pulse format for high power ILC-like beam is 3.2 nC per micropulse at 3 MHz for 1 ms, and the macropulse repetition rate will be 5 Hz. As schematically shown in Fig. 3, this aspect is unique for test facilities in the USA and highly relevant to the next generation of FELs as will be discussed later in this paper. Basic applications of an undulator with ASTA beams are next described with the most significant being the feasibility of an XUV or EUV FEL oscillator being driven by such beams.

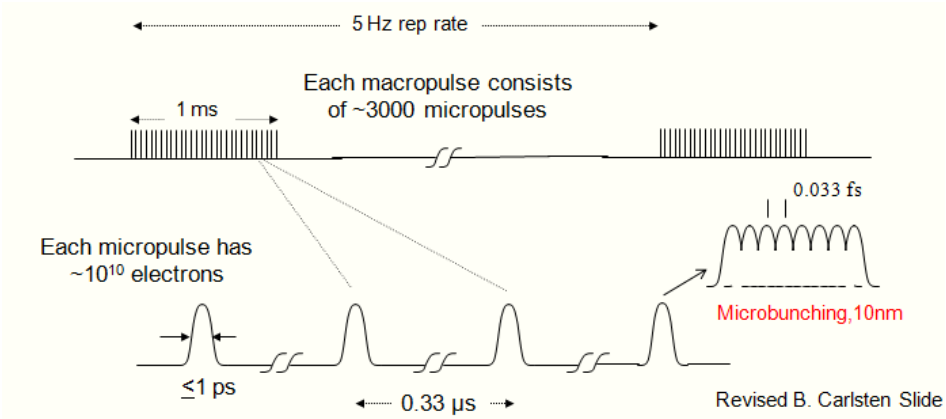

Figure 3: Schematic of the ASTA pulse structure showing the key time scales from ms to μs to ps to fs.

3.9.5 Application 1: Diagnostics Undulator

Initially single-pass operations with an undulator would enable the use of UR properties for deducing time–resolved electron beam properties. The base image size and position will be seen in the UR spot size and transverse position (although the size will have depth-of-focus issues to address. A telescope with limited depth of focus may be used to emphasize a shorter z length within the undulator's 4.5 m length.) The central wavelength of the emission is directly correlated with electron-beam energy, and the bandwidth from the UR will be about 1/nN or 1% for 100 periods at the fundamental. Signal strengths should allow tracking of a subset of the micropulses with standard imaging. The UR pulse length would be measured with the UV-visible C5680 streak camera, and this ps length should be correlated with the electron beam bunch length subject to some narrowing when there is SASE gain. The synchroscan streak camera will also allow tracking of the relative phase within the macropulse of sets of micropulses to about 200 fs. At this time we anticipate one would provide optical transport for the signals to the high

energy end laser lab where a small diagnostics suite of CCD camera, ICCD camera, streak camera, and optical spectrometer would be available on an optics table for characterizing the UR properties and the deduced electron-beam properties. Initial detection could be in the tunnel with local camera stations or detectors.

It is proposed to start studies during the commissioning of the first cryomodule at a beam energy of 125 MeV. As shown in Table I with the 5-cm period and the magnetic gap adjusted for *K*=1.2, the fundamental UR would be at 680 nm with a third harmonic at 226 nm. One could track the beam at higher energies by reducing the gap and increasing the *K* value so that the resonance condition remains in the visible–UV regime to simplify the early tests. One can also consider 150-, 200-, and 250- MeV cases as given in Table I. At 150 MeV the beam could be shared with the injection task for the Integrable Optics Test Accelerator (IOTA) ring tests since the transport lines separate the paths at the high-energy end.

Table I: Summary of possible SER/UR estimated wavelengths predicted with a 5-cm period undulator following the cryomodule(s) at ASTA at 125 MeV and higher electron-beam energies. The last row is for a SC undulator with shorter period built for the ILC R&D program in England [13].

Phase #	Beam Energy (MeV)	Und. Fundamental (nm)	Period (cm), *K*	Undulator Radiation Harmonics (nm) 3, 5
1	125	680	5.0, 1.2	226
1	150 200	472 265	5.0, 1.2 5.0, 1.2	157 88
1 1	250 250	170 262	5.0, 1.2 5.0, 1.8	57 87
2 3 3 4	500 800 800 900	42 16 13.7 3	5.0, 1.2 5.0, 1.2 5.0, 0.9 1.1, 0.9	14, 8.3 5.3 ---

At these wavelengths and for the expected beam quality, the gain length should be sub-m so sufficient SASE-induced microbunching should also occur in the 4.5-m length that could be accessed by demonstrated coherent optical transition radiation (COTR) techniques [11]. In the past these have allowed evaluation and adjusting of the critical electron-beam-photon-beam overlap [12].

In Phase 2 with two cryomodules and a beam energy of 500 MeV, one would need VUV diagnostics since the resonance condition for the fundamental would be at ~42 nm with the third harmonic at 14 nm and the fifth at 8.3 nm. An available in-vacuum flange-mounted 40-

mm diam microchannel plate (MCP) has been identified as a candidate 2D imager that has sensitivity from 1 eV to 50 keV. The output P43 phosphor would be viewed by a standard CCD camera, and two-dimensional images of the VUV UR angular distribution (and CVUVTR if one can block VUV UR) could be recorded. These should indicate laser/e-beam angular overlap which has been shown to impact SIM and FEL gain [12]. The bunch length and phase information could be tracked by collaborating with Dr. B. Yang on use of ANL's Hamamatsu VUV-X-ray streak camera mainframe with FNAL's M5676 synchroscan units tuned to 81.25 MHz. The intrinsic time resolution will not be as good as in the visible regime, but the flexibility for sub-macropulse studies would be maintained as well as system phase stability. Implementation of such a streak camera with a VUV spectrometer is also possible in principle.

Evaluation of the LBNL multilayer metal mirrors at various VUV-XUV wavelengths, and testing of their robustness to photon-beam pulse trains would be of interest. The multilayer mirrors would be located after the downstream dipole to eliminate e-beam bombardment. Development of VUV filtering schemes would also be tested. More detailed harmonic information should be obtained by use of imaging spectrometers in the UV and VUV (McPherson spectrometer version has a series of gratings to use and an imaging array for display). There also may be e-beam emittance effects detectable in the relative harmonic intensities and/or the spectral widths.

3.9.6 Application 2: XUV FEL Oscillator

In a separate proposal section (3.8) the possibility of laser-induced microbunching and high gain harmonic generation (HGHG) FEL R&D at ASTA was explored [14]. In principle the 4.5-m long undulator could be the radiator for seeded FEL tests at 40-50 nm (but probably would not reach saturation). This would require an upstream modulator and chicane to be installed with the appropriate parameters. This is under evaluation, but we will defer further discussion of this aspect here in favor of the more intriguing application: the investigation of a VUV-XUV FEL oscillator configuration. The ASTA pulse train at 3 MHz with a bright electron beam of nominal transverse emittances of 2 π mm mrad, peak current of 300 to 400 A, GeV-scale energy, energy spread of 5 $\times 10^{-4}$ provides the enabling technology. Over two decades ago numerical studies using a ring resonator optical configuration were executed at Los Alamos with the FEL 3D simulation code, FELEX, in the VUV and XUV regimes [3]. This relied on two grazing incidence mirrors on-axis and two off-axis multifaceted mirrors (with 6 facets each) to obtain the individual mirror reflectivities needed in the XUV. This is schematically shown in Fig. 4. They considered operations at 100, 50, 12, and 4 nm. At the time their 90% emittance numbers, which I interpret as 4-sigma values, varied from 31 to 10 π mm mrad (the latter being viewed as speculative at that time, but critical for the 4-nm case). They were using a photo-injected gun and normal conducting L-band rf linac in the plan with 8 nC per micropulse of 20 ps duration and transverse emittances of about 25 π mm mrad [4]. At this time, one can expect to surpass at ASTA even their emittance speculations, albeit with lower charge per micropulse. Although they considered a 1.6-cm-period undulator with low *K* value, we can use higher energies than their 261 MeV to reach the resonance conditions in the 40-50 nm regime with only two cryomodules installed. One notes initial gain length evaluations could be done empirically in the single-pass mode before the final design, and a test of the resonator optical path tuning could be initiated with UV-Visible light with only one cryomodule operating.

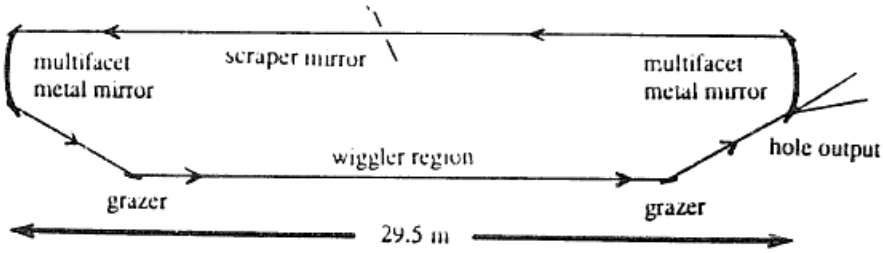

Figure 4: A schematic of the ring optical resonator for an XUV FEL oscillator [2].

One can also consider, in principle, a concentric optical cavity based on two on-axis mirrors with z separation of 50 m (100 m roundtrip) with photons striking at 90 degrees to the surface of the multilayer metal mirrors. If each mirror has ~70% reflectivity as reported for multilayer metal mirrors at LBNL in the XUV regime, the expected gain should exceed the losses. Examples at shorter wavelengths with Mo/Be and Mo/Si multilayers are shown in Fig. 5, and the second case is at the key lithography wavelength of 13.4 nm. Some focusing element would still be needed to provide a Rayleigh range of about 2.2 m for the optical mode. Key issues of spherical aberrations and thermal distortions of the mirrors would be common for all of the designs since absorption of energy is expected in the mirrors. These issues may determine whether a simple concentric cavity would be actually practical.

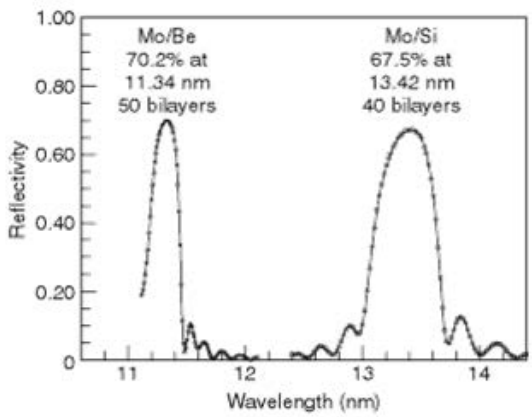

Figure 5: Examples of the reflectivities for multilayer metal mirrors with the incidence angle of 90 degrees to the surface. X-ray Data Booklet, Section 4.1, James H. Underwood, CXRO-LBNL website**.**

In the ring resonator mode the resonator plane would be vertical so the circulating UR would pass just above the undulator. For a 100-m path length resonator, we would need one optical pass to time with the 100-m spacing of the electron beam micropulses at 3 MHz (or one optical pass of 50 m length for a 6-MHz micropulse rate. A single optical pass is definitely preferred so use of the full 50 m in z in the tunnel should be considered. The z length in the beam line would be about 46 m with 2–m distances to the respective off-axis mirrors. In the concentric cavity mode, only two on-axis mirrors are used. A chicane (not shown) could be used to transport the e beam around the left end on-axis mirror location in either case. Figure 6 shows the ring resonator with z-footprint of about 23 m and 50-m optical path (invoking the 6-MHz rate) as it

might fit into one high-energy AARD test area. Note this area is about 42 m downstream of the end of cryomodule 3 and where the chicane might be positioned for the 50-m spacing. (The initial Los Alamos design with two grazers and two multifaceted mirrors is only a little longer at 29.5 m in z for a 60-m round trip path) Simplistically, the gain, G, should satisfy the relation (1+G)(Total reflectivity) > 1 so we need about three gain lengths in the undulator in this case [15]. Based on our previous calculations for SASE gain lengths of about 1 m at 26-40 nm with a different undulator[16], the 4.5-m undulator length should be enough to reach the needed gain and reach saturation in a few hundred passes. Output power coupling of FEL photons was previously proposed by a scraper mirror in one arm of the transport or by a mm-radius hole in one of the mirrors [3,17].

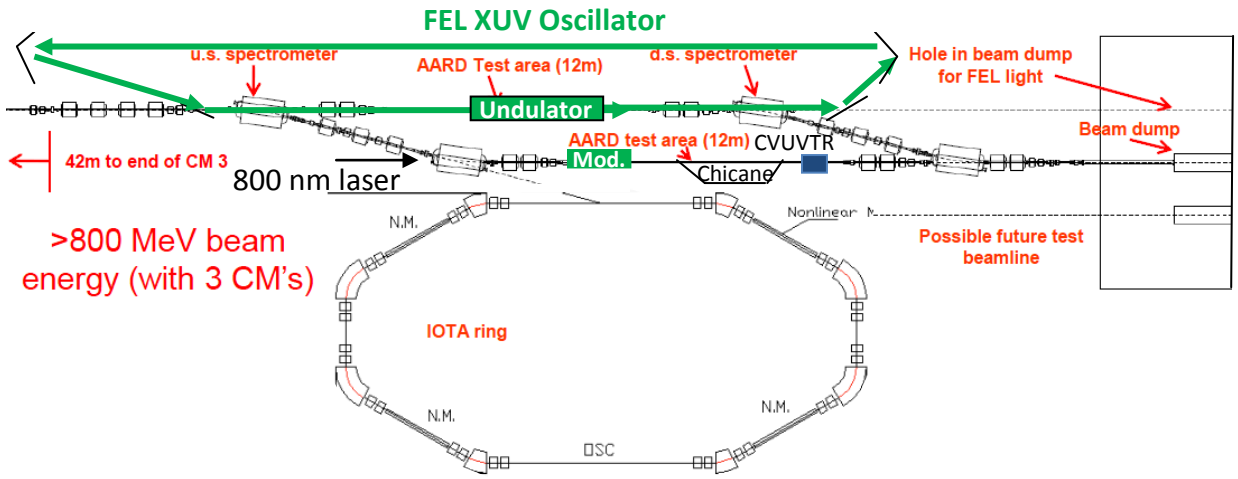

Figure 6: Schematic of the exp[illegible]t layout in one high-energy AARD test area at ASTA for the undulator and XUV FEL oscillator. In the ring resonator mode the resonator plane would be vertical so the circulating UR would pass just above the undulator as if the green arrows in this figure are a side view.

The above are rough estimates so I recently requested modeling of the oscillator properties and parameter dependencies with an existing 1-D particle tracking code with support for oscillators at LBNL. The initial calculations were to be followed by GINGER-based simulations for a subset of conditions as performed at LBNL. The LANL paper had reported a 50-nm FEL case with just a 5-m undulator length [3] so this regime is where we started. The ASTA 42-nm case at 500 MeV beam energy was just evaluated by M. Reinsch (LBNL), and the results are shown in Fig. 7 for a 400-A peak-current value. The cavity was approximated with four reflections with a net power reflectance of $(0.7)^4$. This was a compromise on a single-pass ring resonator estimate. The Beta value assumed was 5 m for the electrons at the undulator. The encouraging results show power gain of 10^5 in 62 passes and saturation after about 100 passes for the 400-A case. The power saturates even sooner for 500- and 600-A cases. The gain length was computed at 1.0 to 1.2 m in the exponential growth regime so the 4.5 m undulator length was needed. The issues of mirror quality, thermal distortions, and mirror damage need also to be addressed. Perhaps the old FELEX code can be used to assess the former issue and newer codes the latter. There is expected to be relevant expertise at LBNL for XUV mirror robustness issues, and the newer mirror cooling techniques may be needed.

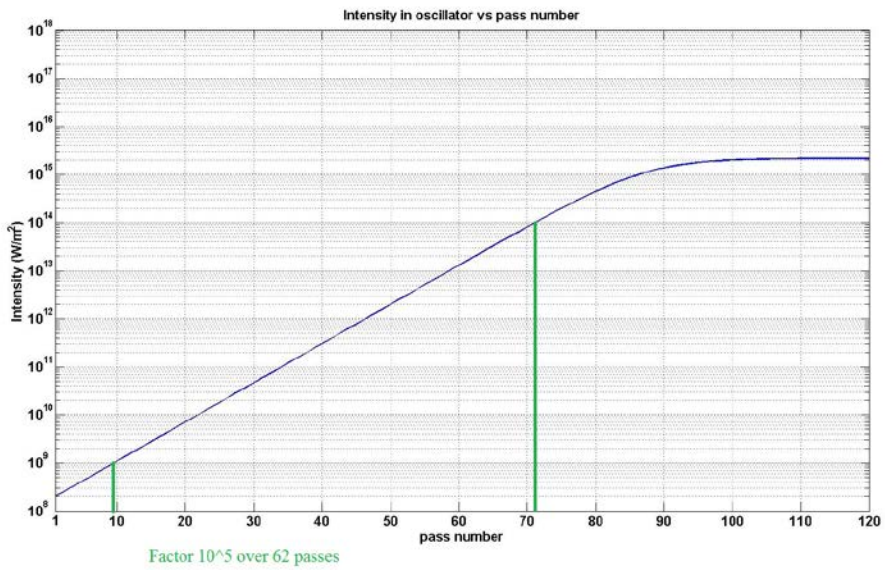

Figure 7: Preliminary FEL oscillator calculational results at 42 nm, using 400 A and 500 MeV beam based on the 1-D particle tracking code with support for oscillators at LBNL. (courtesy of M. Reinsch)

More recently the first GINGER simulations for oscillator cases with projected ASTA beam parameters have been run at LBNL in consultation with M. Reinsch. It appears that in this full simulation, the effective gain length is less optimistic than the 1-D code, but one still can reach output power saturation at 13.4 nm in the concentric cavity case invoking 68% reflectivity at 90 degrees using multilayer metal mirrors. This would occur after about 300 passes in the potential 3000-micropulse train with an 800-A peak current as shown in Fig. 8 for the fundamental and third harmonic. These are only two of the over 20 diagnostics plots from the simulation. After discussion with optics experts at LBNL, surprisingly the solutions for longer wavelengths with multilayer mirrors are estimated at only 40-50% reflectivity. The multifacet mirror concept may thus be the primary solution for broadband tunability of the FEL and remains a critical R&D topic.

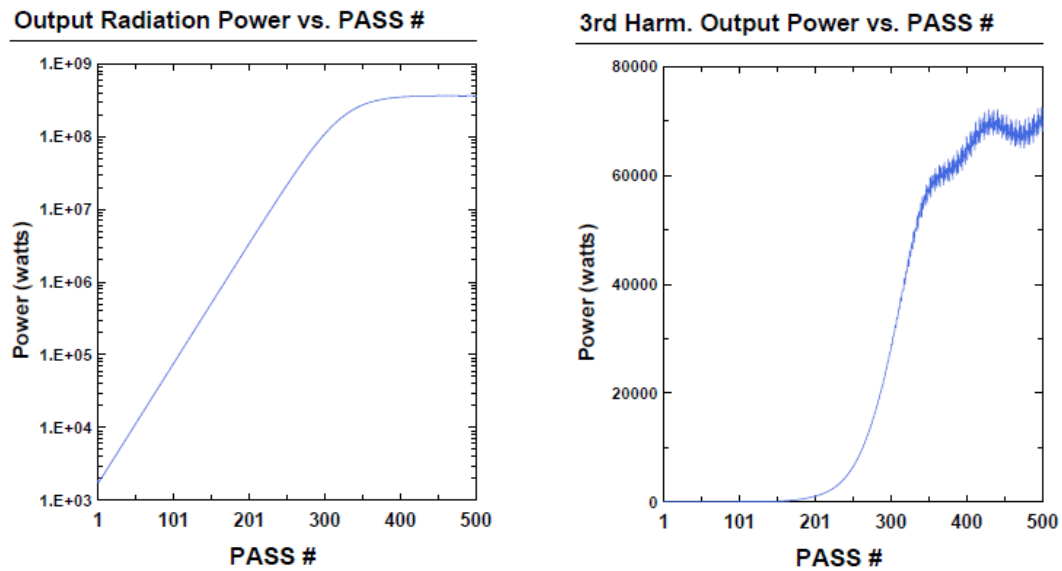

Figure 8: Initial GINGER simulations for output power saturation at the fundamental 13.4-nm wavelength (left) and the third harmonic (right) for a concentric cavity with multilayer mirrors and peak current of 800 A at 800 MeV. The output power growth with pass number is shown. (courtesy of M. Reinsch)

There is a significant opportunity for this FEL oscillator R&D that can uniquely be done at ASTA in the USA. It is one possible configuration of the next generation of light sources with the potentially narrower bandwidths (transform limited) needed by some science cases, and should complement the seeded and self-seeded FEL configurations. Demonstration of an FEL oscillator at even 40-50 nm would shatter the existing world record of ~180 nm [8]. With higher energies and shorter period undulators the few-nm regime should be attainable in principle as roughly scaled in the Phases 3 and 4 of Table I, assuming the ring resonator concept with multifaceted mirrors is viable and/or cooled mirrors are used.

3.9.7 Practical Considerations

The two investigation areas provide a compelling case for consideration of installing such an undulator in ASTA. We currently have an option for the U5.0 device [18] that is being retired from the ALS storage ring in January 2013. There are some practical considerations, however, mostly driven by the labeled weight of 47,000 lbs which is close to the NML crane's 25-ton capacity. The undulator has a 5.0-cm period, 4.5-m magnetic structure length, a maximum field strength of 0.87 T at 1.4-cm gap, and a remotely controlled adjustable gap from 1.4 to 21.4 cm leading to a range of *K* values. The strong back and the specification to have the device's gap constant to about 50 µm over the 4.5 m length leads to the very substantial support structure. Its total height is 2.4 m as compared to the ASTA tunnel height of 3.2 m (10.5 ft). The vacuum chamber is 5.1 m flange to flange and has an antechamber. As staged at ALS, the beamline centerline is at ~55 inches, higher than our ASTA beamline center of 48 inches. There appears in reference [18] to be a baseplate under the frame of about 15 in. height that might be shortened. These should be evaluated for modification, or we have to shift the beam trajectory upward with a dogleg in this area. Two photographs of the device in situ from M. Wendt's visit

to LBNL in April 2012 are shown in Fig. 9, and initial device characterizations were previously reported [19]. I don't believe there are any diagnostics or quadrupoles embedded within the structure's length. The mechanical, vacuum, and gap control aspects should be still evaluated by experts at FNAL.

Figure 9: Photographs of the ALS U5.0 Undulator in the storage ring in April 2012. (from M. Wendt)

It is conceivable that in 4-6 years some APS undulator-A's with 3.3-cm period and 2.4-m length would be retired at APS after the APS-Upgrade, and some *might* then become available. Perhaps we should put in a bid now. Also, the estimated cost for a 1–m length permanent magnet device, 2-cm period, and with fixed gap (as I recall) was $125 k with a 12-15 month lead time based on discussions with undulator-cognizant staff at ANL and LBNL in 2011. The permanent magnets themselves have been on a 12-month lead time from Japan for many months. There is a flexible magnet design with 2.4-cm period at Cornell [20], but at the moment no 4.5-m-long device to borrow. The ALS U5.0 option costs FNAL the shipping, installation, and controls time, but the device replacement value is over $2M (per M. Wendt). In the present budget climate, an undulator in hand is worth two elsewhere……or priceless.

3.9.8 Summary

In summary, we have described applications at ASTA of a 5-cm period undulator with 4.5-m length *and* tunable magnetic gap including: 1) non-intercepting e-beam diagnostics using UR during commissioning of the first cryomodule and 2) the magnetic structure for the *first* XUV FEL oscillator in the world. Although the ALS device may not be optimized for each application, its presence would jump start photon-related research at ASTA and support initial FEL oscillator tests at ~40 nm and perhaps 13.4 nm later. In the future, use of shorter period (1.8 cm) permanent magnet devices or existing 1.1-cm-period SC devices and higher beam energies would allow us to push to few-nm wavelengths and soft x–rays which should be of interest to the next-generation-of-light-source strategies (and consequently DOE/HEP, DOE/BES, and the National Science Foundation). The experiments should drive mirror technology implementations, XUV detector development, and preliminary basic science experiments that need transform-limited coherent photon sources of sub-ps duration as consistent with the identified mission needs of DOE. This would be a highly leveraged test program since the major

infrastructure of the SCRF linac is assumed as given and an undulator transfer negotiation is underway. The oscillator cavity and some detectors are the incremental costs and estimated as a fraction of the replacement value of the undulator.

3.9.9 Acknowledgements

The author acknowledges discussions with: M. Wendt, M. Church, H. Edwards, S. Nagaitsev, and S. Henderson of FNAL on the ASTA facility and the AARD program; R. Lindberg (ANL), M. Reinsch (LBNL) and J. C. Goldstein (LANL, retired) on FEL oscillators; and J. Ruan of FNAL on UV-Visible optical considerations.

Notes: Installation of 1-3 cryomodules assumed with transport of beam to the high energy beam dump. The details of the soon-to-be-retired ALS U5.0 undulator's transfer to FNAL are ongoing. The mirror chambers are estimated at $25k each for single mirrors with piezo adjustments for the initial concentric UV case. The ring resonator with multifacet mirrors needs further evaluations. A diagnostics suite would also be needed, but initially an existing in-vacuum MCP with standard camera, and YAG:Ce or LYSO:Ce scintillator crystals with photo detectors could be used. A VUV-XUV spectrometer would be needed to evaluate laser performance.

3.9.10 References

1. Sergei Nagaitsev, "ILC-TA at NML", ILC-TA Workshop at Fermilab, November 2006; J. Leibfritz, "Status of Plans for a Superconducting RF Test Facility at Fermilab", Proc. of IPAC12, May 2012.
2. "Realizing the Potential of Seeded Soft X-ray FELs Workshop", hosted by LBNL and SLAC, Berkeley CA, Oct. 26-28, 2011.
3. John C. Goldstein, Brian. D. McVey, and Brian E. Newman, Nucl. Instr. and Methods in Phys. Research A296, 288 (1990).
4. B.E. Carlsten, Nucl. Instr. and Methods in Phys. Research A285, 313 (1989).
5. Alex H. Lumpkin, Nucl. Instr. and Methods in Phys. Research A296, 134-143 (1990).
6. E. Tarazona and P. Ellaume, Rev. of Sci. Instrum. **66**, 1974 (1995).
7. Alex H. Lumpkin and Bingxin Yang, Phys. Rev. Letters, Vol. 82, No. 18, May 3, 1999, pp. 3605-3608.
8. F. Curbis et al., Proc. of the 27th FEL Conference, 473, JACoW econf, (2005).
9. Based on D. Moncton slide at the WIFEL Workshop in Oct. 2007 and the original paper by R. Bonifacio,C. Pelligrini, and L. Narducci, Opt. Commun. 50,373 (1984).
10. P. Musumeci, C. Pellegrini, and J.B. Rosenzweig, Phys. Rev. E **72**, 016501 (2005).
11. A.H. Lumpkin et al., PRL **88**, 234801, (2002).
12. A. H. Lumpkin et al., Proceedings of the 25th FEL Conference, Tsukuba, Japan, Sept. 8-12, 2003, NIMA 528, pp. 179-183 (2004).
13. E. Baynham et al., Proc. of PAC09, WE2RAIO1 (2009).
14. A. H. Lumpkin, J. Ruan, J. M. Byrd, and R. Wilcox, " Potential for Critical Laser-Induced Microbunching Studies with the High-Micropulse-Repetition Rate Electron Beams at ASTA", DocDB Fermilab Dec. 2011.
15. R. Lindberg (private communication, June 2012).

16. A.H. Lumpkin, M. Church, H. Edwards, S. Nagaitsev, and M. Wendt, "Considerations on Fermilab's Superconducting Test Linac for an EUV/Soft X-ray SASE FEL", Proc. of FEL10, JACoW, (2010).
17. Neil Thompson et al., "The 4GLS VUV-FEL", 29-03-07.
18. E. Hoyer et al., Rev, Sci. Instrum. 63 (1), 359 (1992). This paper describes the ALS U5.0 design.
19. P. Heimann et al., Rev, Sci. Instrum. 66 (2), 1885 (1995).
20. A. Temnykh, Proc. of PAC09, MO6PFP084, 324, JaCoW (2009).

3.10 Production of narrow-band gamma rays

This experiment has been proposed by Muons, Inc. Basic concept is shown in Figure below:

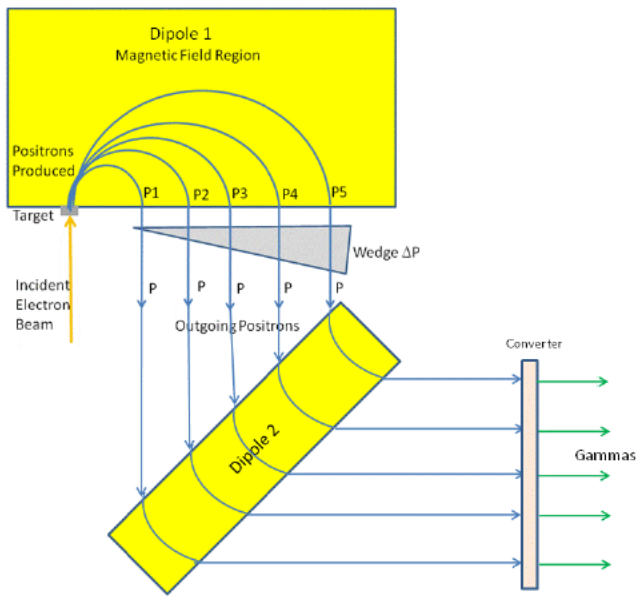

"Project Gamma" has been developed under a contract with Pacific Northwest National Lab. A Preliminary Conceptual Design Document for a proof-of-principle experiment has been completed in 2012. It includes results of a complete end-to-end simulation of the system. More detail could be provided by request.

In 2011, Muons Inc. has submitted an expression of interest to Fermilab.

3.11 Synergies with the MAtter-Radiation Interaction at the Extreme (MARIE) project at Los Alamos

LANL MARIE's project team has approached Fermilab with request to carry out some relevant beam dynamics experiments at ASTA. The proposal and plan are being formulated with expectation to be submitted later in 2012.

3.12 Beam-Beam Kickers for ELIC at JLab

(Zhang, Derbenev) http://casa.jlab.org/research/elic/elic.shtml

3.13 Radiabeams on Gamma-Source

(Murokh)

3.14 Space Charge Compensation

(M. Chung – FNAL)

3.15 Demonstration of Technology and Beam Parameters of an ILC RF-unit

(Marc Ross, Solyak/Yakovlev)

3.16 Miscellaneous Expressions of Interest

As Fermilab's ASTA User's program plans become more and more widely known to accelerator community, we receive new expressions of interest. E.g., at the FEL11 conference in Shanghai and the "Seeded FELs" Workshop at LBNL (October 2011), several preliminary discussions with LANL, LBNL, SLAC, DESY, and SINAP staff in regard to possible experiments to be done at ASTA had taken place. Most of their interests fit the beam manipulation category and several experiments could be done at ASTA at 40 MeV:

1. on double emittance exchange to generate short bunches or a flat beam transform followed by a wedge filter or canted wiggler for low emittance (B. Carlsten and K. Bishofsberger of LANL)
2. on slice emittance studies following chicane beam compression at 40 MeV to validate his model (J. Qiang of LBNL)
3. on testing of reversible beam heating and suppression of microbunching with two transverse deflecting mode cavities on either side of a chicane compressor (Z. Huang, C. Behrens (DESY), and D. Xiang of SLAC)
4. on use of seeding schemes for inducing narrowband microbunching at ASTA (Z. Zhao of SINAP)

It was also mentioned that the microbunching instability mechanisms continue to present challenges in the bright beam community and are a good topic to explore, and that ASTA is a uniquely fit facility in the US to study these topics.

4.0 The Fermilab Context

Accelerator R&D has played a crucial role in enabling scientific discovery in the past century and will continue to play this role in the years to come. In the U.S., the Office of High Energy Physics of DOE's Office of Science is developing a plan for national accelerator R&D stewardship.

Fermilab undertakes accelerator research, design, and development focused on superconducting radio-frequency (RF), superconducting magnet, beam cooling, and high intensity proton technologies. In addition, the Laboratory pursues comprehensive integrated theoretical concepts and simulations of complete future facilities on both the energy and intensity frontiers. At present, Fermilab (i) supplies integrated design concept and technology development for a multi-MW proton source (Project X) to support world-leading programs in long baseline neutrino and rare processes experiments; (ii) plays a leading role in the development of ionization cooling technologies required for muon storage ring facilities at the energy (multi-TeV Muon Collider) and intensity (Neutrino Factory) frontiers, and supplies integrated design concepts for these facilities; and (iii) carries out a program of advanced accelerator R&D (AARD) in the field of high quality beam sources, and novel beam manipulation techniques.

To expand the advanced accelerator R&D effort, we plan to leverage on the ILC test accelerator currently under construction in the New Muon Lab (NML) building at Fermilab. The facility is configured to eventually produce electron beam with energies close to 1 GeV. Fermilab is therefore envisioning this facility, the Advanced Superonducting Test Accelerator (ASTA), will eventually support a vibrant user-driven research program in Accelerator Science and beyond. The purpose of the present report is to summarize the current plan for ASTA.

5.0 Technical Description of ASTA

6.0 Accelerator Science Education at ASTA

7.0 Scope, Cost and Schedule

8.0 Operating Budget

8.1 Assumptions

9.0 Management of the Scientific User Program

The organization of the AARD program is planned to be established in 2013. Under guidance of a Program Director (search is currently underway - see Appendix A), the experiments will be evaluated at the stage of proposals by an external Program Committee consisting of

internationally recognized scientists and will be set up and carried out at ASTA by users in collaboration with Fermilab's operational and scientific staff - see the org-chart below.

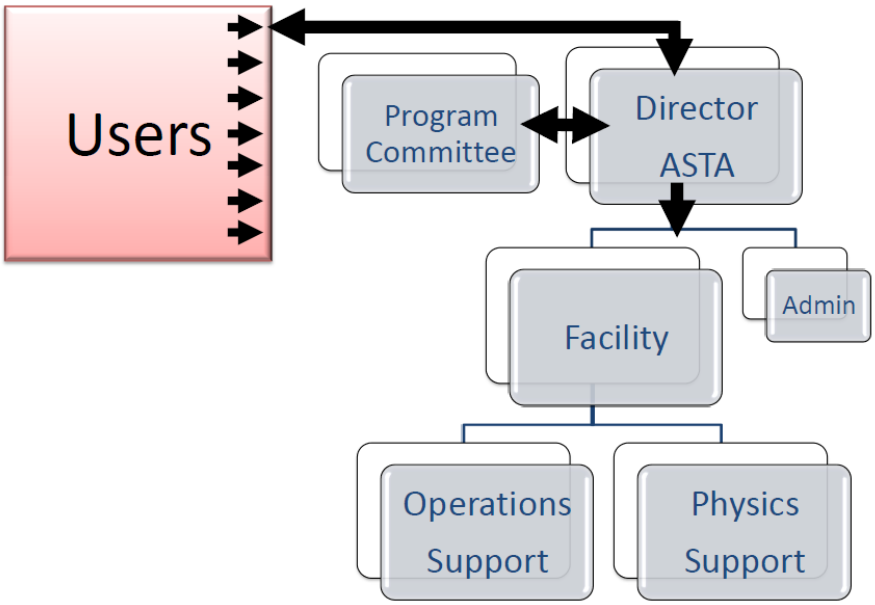

Proposed organizational structure of the ASTA AARD User's Facility Program

10.0 List of Acronyms – new 7/30

ASTA: Advanced Superconducting Test Accelerator
EEHG: echo-enhanced harmonic generation
FEL: free-electron laser
HGHG: high-gain harmonic generation
HHG: high harmonic generation
LIM : laser-induced microbunching
LSCIM: longitudinal-space-charge-induced microbunching
OPA: optical parametric amplifier
OTR: Optical transition radiation
COTR: coherent OTR
CVUVTR: coherent vacuum ultraviolet transition radiation
SASE: self-amplified spontaneous emission
SIM: SASE-induced microbunching

11.0 Appendix 1: Letters of Support

12.0 References – apparently this must be last to work!

[1] DESY gun
[2] J. Ruan, H. Edwards, R. P. Fliller III, J. K. Santucci, Proceedings of PAC07, Albuquerque, New Mexico, USA, 470 (2007).
[3] P. Piot, Phys. Rev. Lett. **108**, 034801 (2012) (submitted 2011)
[4] P. Piot IPAC10 (2010).
[5] T. Maxwell EOS
[6] C. Brau, B. Choi, J. Jarvis, J. W. Lewellen and P. Piot, to appear in Synchrotron Radiation News, issue of January 2012.
[7] M. A. Kumakhov, Phys. Lett. **A 57**, 17 (1976).
[8] R. W. Terhune and R. H. Pantell, Appl. Phys. Lett **30**, 265 (1977).
[9] W. Wagner, B. Azadegan, M. Sobiella, J. Steiner, K. Zeil, and J. Pawelke, Nucl. Instrum. Meth. **B 266**, 327 (2008).
[10] M. A. Kumakhov, International Conference on Charged and Neutral Particles Channeling Phenomena, edited by S. B. Dabagov, Proc. SPIE 5974, (SPIE, Bellingham, WA, 2005).
[11] B. Azadegan, Ph.D. thesis, Technischen Universität Dresden, 2007.
[12] C. K. Gary, R. H. Pantell, M. Ozcan, M. A. Piestrup, and D. G. Boyers, J. Appl. Phys. **70**, 2995 (1991).
[13] W. Neubert, B. Azadegan, W. Enghardt, K. Heidel, J. Pawelke, W. Wagner, Nucl. Instrum. Meth. B **254**, 319 (2006).
[14] C. Brau, Private communication (2011)
[15] J. D. Jarvis, H. L. Andrews, C. A. Brau, B.-K. Choi, J. Davidson, W.-P. Kang, and Y.-M. Wong, J. Vac. Sci. Technol. **B 27**, 2264 (2009).
[16] J. D. Jarvis, H. L. Andrews, B. Ivanov, C. L. Stewart, N. de Jonge, E. C. Heeres, W.-P. Kang, Y.-M. Wong, J. L. Davidson, and C. A. Brau, J. Appl. Phys. **108**, 094322 (2010).
[17] J. W. Lewellen and J. Noonan, Phys. Rev ST Accel. Beams 8, 033502 (2005).
[18] H. Boersh, Ziet. Physik, 139, 115-146 (1954).
[19] M. Krueger, M. Schenk, and P. Hommelhoff, Nature **475**, 77 (2011).
[20] D. A. Edwards, LINAC 2002
[21] Y.-E Sun, Phd Thesis
[22] Y.-E Sun, PRTAB 2004
[23] P. Piot, PRSTAB2006
[24] T. Koeth, PAC2009
[25] J. Ruand et al., PRL 2011
[26] Y.-E. Sun, et al., PRL 2010
[27] P. Piot, et al. APL 2011
[28] B. Carlsten, et al. ArXiV paper
[29] P. Emma, Piot, Kim PRSTAB 2006
[30] Kim Flat beams
[31] Cornacchia and Emma PRSTAB 2004

[32] P. Piot, proceeding of AAC08 (2009).
[33] MacAshan + Rainer (TM memo- (2011).
[34] Zholents ANL/APS/LS-321, May 2011 (2011).
[35] V. Danilov and S. Nagaitsev, Phys. Rev. ST Accel. Beams 13, 084002 (2010).
[36] N. Nekhoroshev, "Behaviour of Hamiltonian systems close to integrable", Functional. Anal. Appl. 5 (1971), 338–339
[37] G. Darboux, "Sur un problème de mécanique", Arch. Néerlandaises Sci., Vol. 6, 371–376 (1901).
[38] S. Nagaitsev et al., in Proceedings of HB2010, Morschach, Switzerland (2010), THO1D01.
[39] A. Valishev et al., in Proceedings of PAC11, New York, NY (2011), WEP070.
[40] I. Batalov, A. Valishev, Fermilab Beams-doc-3959 (2011).
[41] D. Shatilov et al., Phys. Rev. ST Accel. Beams 14, 014001 (2011).